# Direct generation of structured light beams from solid-state lasers

# 多様な特殊波面モードをレーザー発振する固体レーザーの開発

August 2020

YUANYUAN MA

Graduate School of

Science and Engineering

CHIBA UNIVERSITY

(千葉大学審査学位論文)

# Direct generation of structured light beams from solid-state lasers

# 多様な特殊波面モードをレーザー発振する固体レーザーの開発

August 2020

YUANYUAN MA

Graduate School of
Science and Engineering

CHIBA UNIVERSITY

# Acknowledgments

I would like to thank all the people who helped my whole research life and supported me during my Ph.D. project period.

In particular, I would like to thank my supervisor, Prof. Takashige Omatsu, for his ongoing support of the research and guidance and for allowing me to study under his laboratory. During these four years, he gave me an abundant guide on my presentations and writing papers. So, here, I would thank him from the bottom of my heart for his selfless dedication.

Also, I would like to thank Dr. Adam Vallés for providing insightful technical input in experimental and theoretical discussions. And a special thanks goes to Dr. Jung-Chen Tung for providing assistance in understanding the experimental concepts.

I am further grateful to Dr. Andrew. J. Lee (Macquarie Univ.), Prof. Helen. M. Pask (Macquarie Univ.), and Dr. Yameng Zheng (Macquarie Univ.), for all their guidance and help, when I studied at Macquarie University.

I would like to especially thank Dr. Miyamoto, Dr. Toyoda Kohei, Tsukamoto for their all kinds of help in life, so I had a great four years.

In addition, in the past four years, thank you for being with me, Junhyung Lee, Keigo Masuda, Roukuya Mamut. We discussed and studied together and participated in academic conferences together. Your positive attitude has always inspired me. I also want to thank my seniors, Ablimit Ablez, Shungo Araki, and Yuta Sasaki, for their greatest help when I first came to Japan. Besides, I would thank all members of the Omatsu-Miyamoto group, for their useful discussions and precious help during these four years. Thanks to your guys Shigeki Nishida, Kazuki Sano, Shunsuke Toyoshima, Shogo Nakano, Koki Yamaguchi, Tomohito Yamasaki, Fukutaro Shiraishi, Takanori Kineduka, Jun Shibakawa, Tatsuyuki Sugimoto, Yuri Nakamura, Takahiro Miyakawa, Ayan Ayane Murakami, Jiahuan He, Mirzati Purati, Ryo Shinozaki, Ryusuke Nakamura, Kenshiro Ninuma, Masaki Furuta, and Reimon Matsuo.

Finally, I would like to deeply thank my parents and my sister for their financial and emotional support during my educational pursuits as well as their self-giving love. Without their support, I would probably not finish my Ph.D. course.

# Abstract

A myriad of structured-light beams generated in the laser systems have been widely investigated in versatile applications, such as optical trapping, high spatial resolution microscopy, free space telecommunication with high data capacity, and laser materials processing. To explore further the research opportunities of such structured-light beams, this paper aims to present the direct generation of structured-light beams, including the 2D optical vortex beams, and the 3D bottle beam, from solid-state laser systems.

Firstly, I report on a continuous-wave self-Raman Nd:$GdVO_4$ vortex laser based on two Raman shifts of 382 $cm^{-1}$ and 882$cm^{-1}$ by shaping the pumping beam shape via an axicon lens and a focusing lens. Selective generation of infrared vortex beams with zero orbital angular momentum (OAM) at 1.108 μm or 1.173 μm, or both 1.108 μm and 1.173 μm, was achieved by simply aligning the output coupler in the resonator. The maximum Raman vortex output powers at the wavelengths of 1. 108 μm (the first-Stokes emission of the 382 $cm^{-1}$ Raman shift) and 1.173 μm (the first-Stokes emission of the 882 $cm^{-1}$ Raman shift) were then measured to be 49.8 mW and 133.4 mW at the absorbed pump power of 5.69 W, respectively. A numerical analysis based on the incoherent superposition of two Laguerre-Gaussian (LG) mode beams with opposite helical wavefronts supported well the experiments. Such vortex laser sources will be extended to develop visible and ultraviolet (UV) vortex laser systems to fill in a wavelength gap of solid-state lasers.

Secondly, I perform the direct generation of red and orange (640 nm and 607 nm) vortex outputs by using an off-axis pumping configuration in a diode-pumped trivalent praseodymium ions doped yttrium lithium fluoride ($Pr^{3+}$:YLF) laser. The generated structured light beams can be supported well by a detailed numerical analysis based on the coherent superposition of Hermit-Gaussian modes with different amplitudes and relative phases. The maximum red and orange vortex output powers were measured to be 808 mW and 211 mW at a pumping power of 3.16 W, respectively. The handedness control of the generated vortex beam was also demonstrated. Such compact visible vortex laser sources will be potentially applied in the scanning fluorescence microscopes and micro-fabrications with high spatial resolution beyond diffraction limit.

Thirdly, I demonstrate the generation of ‘bottle beam’ with a 3 dimensional dark (null intensity) zone, consisting of a series of frequency-locked LG modes, from a compact intracavity frequency-doubled Nd:$YVO_4$ laser with a nearly hemispherical cavity. The generated bottle beam then manifests several times higher potential barrier with narrow trapping width than that in other proposed approaches.

Finally, I summarize the key issues of the experimental and numerical works presented in this thesis, and mention briefly the potential avenues of future work.

# Table of Contents

# List of Figures

## Chapter. 1



## Chapter. 2



## Chapter. 3

## Chapter. 4



## Chapter. 5

## Chapter. 6

## Chapter. 7



## Chapter. 8

# Publications

[1] J. C. Tung, **Y. Y. Ma**, K. Miyamoto, Y. F. Chen, T. Omatsu, "Bottle beam generation from a frequency-doubled Nd:$YVO_4$ laser," Sci. Rep. **8**(1), 16576, (2018).
(**Equally contributed first co-author**)

[2] **Y. Y. Ma**, A. Vallés, J. C. Tung, Y. F. Chen, K. Miyamoto, and T. Omatsu, "Direct generation of red and orange optical vortex beams from an off-axis diode-pumped $Pr^{3+}$:YLF laser," Opt. Express **27**(13), 18190-18200 (2019).

[3] **Y. Y. Ma**, A.J. Lee, H. Pask, K. Miyamoto, and T. Omatsu, "Direct generation of 1108 nm and 1173 nm Laguerre-Gaussian modes from a self-Raman Nd:$GdVO_4$ laser," Opt. Express **28**(16), 24095-24103 (2020).

# International conferences

[1] J. C. Tung, **Y. Y. Ma**, Y. F. Chen, K. Miyamoto, T. Omatsu, "Bottle beam generation from a frequency-doubled Nd:$YVO_4$ laser with a tightly end-pumping geometry," Proc. SPIE 10712, Optical Manipulation Conference, paper 107120O, Yokohama, Japan (2018).

[2] J. C. Tung, **Y. Y. Ma**, Y. F. Chen, K. F. Huang, and T. Omatsu, "Direct generation of a 'bottle beam' from an end-pumped Nd:$YVO_4$ laser with second-harmonic generation," Conference on Lasers and Electro-Optics (CLEO:2018), paper SF3I.8, San Jose, USA (2018).

[3] **Y. Y. Ma**, J. C. Tung, K. Miyamoto, Y. F. Chen, and T. Omatsu, "High-order bottle beam from a frequency-doubled Nd:$YVO_4$ laser," JSAP-OSA Joint Symposia 2018, paper 20a_211B_6, Nagoya, Japan (2018).

[4] **Y. Y. Ma**, J. C. Tung, K. Miyamoto, and T. Omatsu, "Direct generation of bottle beam from a frequency-doubled Nd:$YVO_4$ laser," 2018 Joint Symposia on Optics, paper 31aCJ6, Tokyo, Japan (2018).

[5] **Y. Y. Ma**, J. C. Tung, Y. F. Chen, K. Miyamoto, T. Omatsu, "Visible vortex light source based on a diode-pumped $Pr^{3+}$:YLF lasers," Optical Manipulation Conference, paper 11141, Yokohama, Japan (2019).

[6] **Y. Y. Ma**, J. C. Tung, K. Miyamoto, and T. Omatsu, "Direct generation of vortex beams from a diode-pumped $Pr^{3+}$:YLF laser," Conference on Lasers and Electro-Optics

(CLEO:2019), paper JTu2A.62, San Jose, USA (2019).

[7] **Y. Y. Ma**, J. C. Tung, Y. F. Chen, A. Valle-Mari, K. Toyoda, K. Miyamoto, and T. Omatsu, "Handedness control of visible optical vortex output from a diode-pumped $Pr^{3+}$:YLF laser," Conference on Lasers and Electro-Optics Europe and European Quantum Electronics Conference (CLEO/EQEC 2019), paper ca_1_5, Munich, Germany (2019).

[8] **Y. Y. Ma**, A. Vallés, K. Miyamoto, and T. Omatsu. "Diode-pumped red-orange vortex $Pr^{3+}$:YLF laser," JSAP-OSA Joint Symposia 2019, paper 21a_E214_1, Hokkaido, Japan (2019).

[9] **Y. Y. Ma**, A. J. Lee, H. Pask, and T. Omatsu, "1108 nm vortex mode generation from a self-Raman Nd:$GdYO_4$ laser," Conference on Lasers and Electro-Optics (CLEO:2020), paper JW2B.1, San Jose, USA (2020).

# 1 Introduction

## 1.1 Structure light beam

Versatile structured light beams have been gradually proposed, so far, and they are currently becoming a ‘hot’ subject of interest [1-6]. Such structured light beams were earlier demonstrated as a series of spatial eigen modes in lasers [7-10]: for instance, some stationary and dynamic transverse lasing modes were demonstrated in [1,5].

In 1992, Allen et al. proposed theoretically the light field with an orbital angular momentum (OAM), that is an optical vortex, associated from a null field amplitude and an on-axis phase singularity assigned by a topological charge [10-13]. In 2000, Arlt and Padgett proposed an “bottle beam,” possessing a three-dimensional (3D) dark core surrounded by bright regions [14].

Such structured light beams, such as optical vortices and bottle beams have been attracting great research popularities and activities in diverse fields, such as optical communications, quantum optics, optical metrology, optical manipulations, and high-resolution microscopy. To date, there are many technologies to generate the desired structured light beams. The direct generation of the structured light beams from solid-state laser technologies is a promising and efficient approach to produce the oscillation of preferential spatial mode as eigen modes with high power and beam quality.

In this thesis, I focus on the generation of optical vortex and bottle beams based on solid-state laser technologies.

## 1.2 Optical vortices and their applications

Optical vortex beams [10,15-19] possess an annular spatial profile (with an on-axis intensity dark core) carrying a nonzero OAM of $\ell\hbar$ per photon, where integer $\ell$ (positive or negative) is the topological charge, owing to their on-axis phase singularity. Laguerre–Gaussian (LG) modes, the most conventional optical vortex beams, are the eigen modes, that is their spatial forms remain unchanged during the space propagation, of the paraxial electromagnetic equation in the cylindrical coordinate system. Figure 1.1 shows the illumination of the optical vortex.

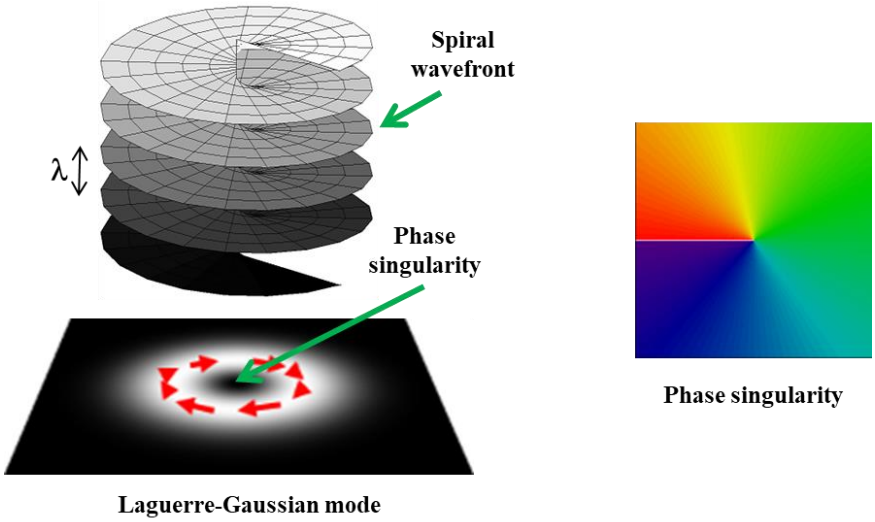


Fig. 1.1 Basic concept of the optical vortex

Optical vortex beams enable us to physically twist various materials [20-25], including metal, silicon, azopolymer, and photo-polymerized cure resin towards a clockwise or counter-clockwise direction, thereby yielding chiral structured materials on a nano or micron scale.

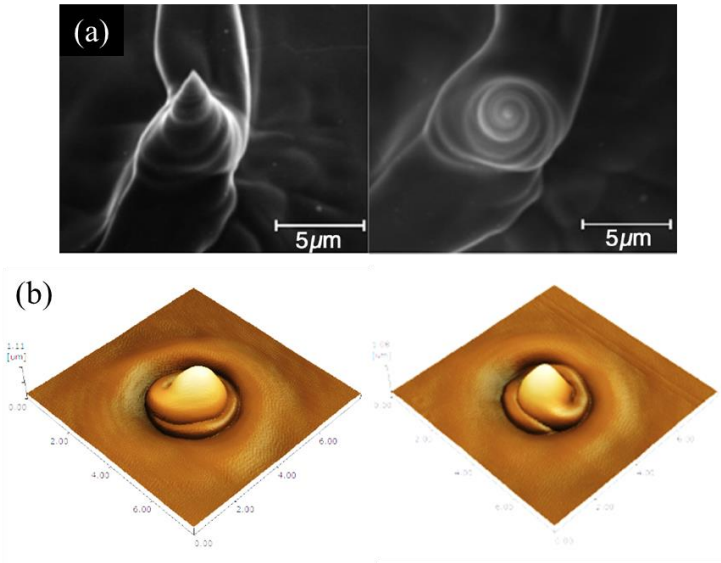


Fig. 1.2 Twisted structures fabricated on (a) tantalum substrates and (b) azo-polymer thin films.

Also, optical vortex beams allow us to significantly improve the spatial resolution of laser scanning fluorescence microscopes far beyond the diffraction limit [26-28], in which the optical vortex beams act as an erase beam of the fluorescence signal from the irradiated target through stimulated emission or higher up-conversion excitation.

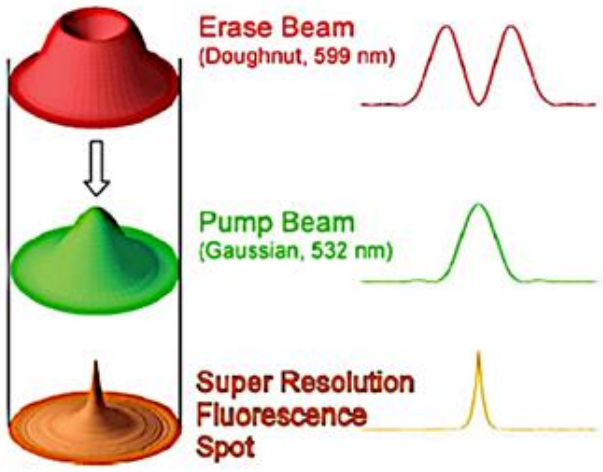


Fig. 1.3 Schematic diagram of the scanning fluorescence microscopy with high spatial resolution beyond the diffraction limit (dubbed 'super-resolution microscope').

Further, optical vortex beams have been significantly attracting research interests in quantum information and communication [29-35], in which the optical vortex beams with the freedom of OAM states increase data capacity and spectral efficiency.

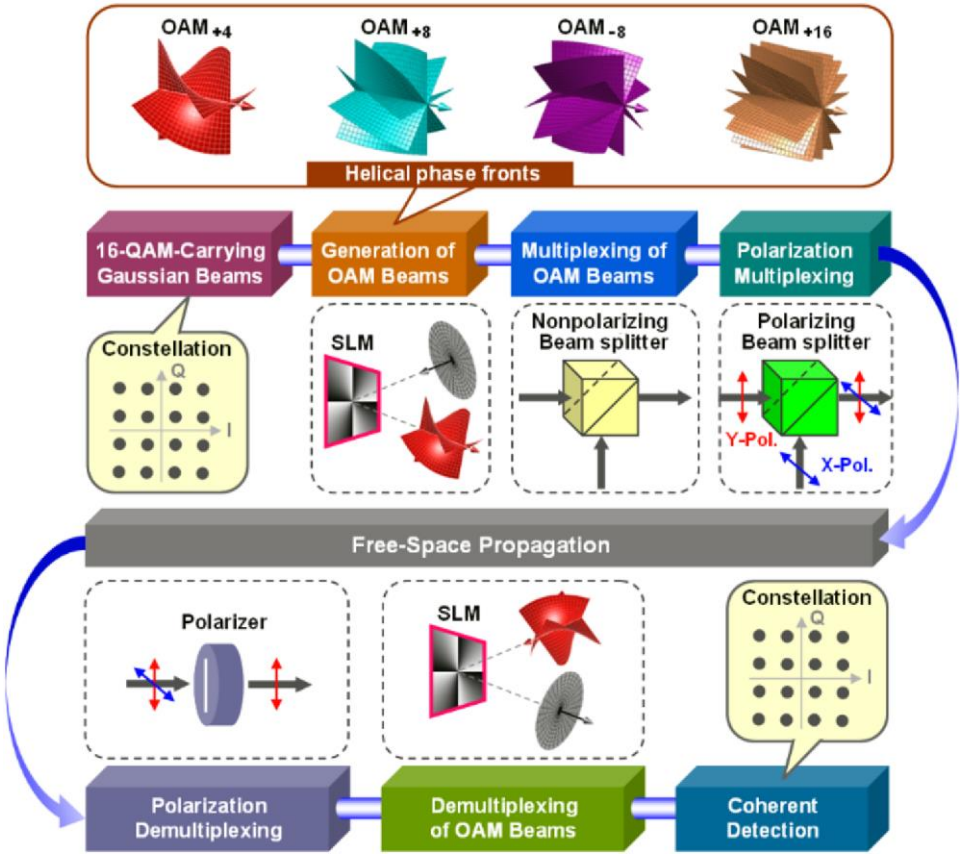

Fig. 1.4 Free-space optical communications based on the spatial multiplexing/demultiplexing of optical vortices with different OAM states in combination with polarization multiplexing/demultiplexing techniques.

To realize the aforementioned demonstrations and applications, it is strongly necessary to develop optical vortex sources with wavelength versatility for exactly the same reason that wavelength versatility is needed in applications of conventional laser sources.

## 1.3 Bottle beams and their applications

The bottle beam is, in general, formed of a coherent superposition of two high-order radial LG beams with their azimuthal indices $\ell = 0$ and their non-zero radial indices, for instance, $p = 0$ and $p = 2$, and it exhibits a central bright spot in both near and far-fields and an on-axis dark core in the middle region between the near and far-fields, as shown in Fig. 1.5.

The LG beams with $\ell > 0$ or high-order Bessel beams, eigen modes of the electro-magnetic equation, also exhibit on-axis null core, however, their intensity profiles remain unchanged even during the beam propagation. Thus, the bottle beams, formed of superpositions of two or more eigen modes with relative phase, are not eigen states.

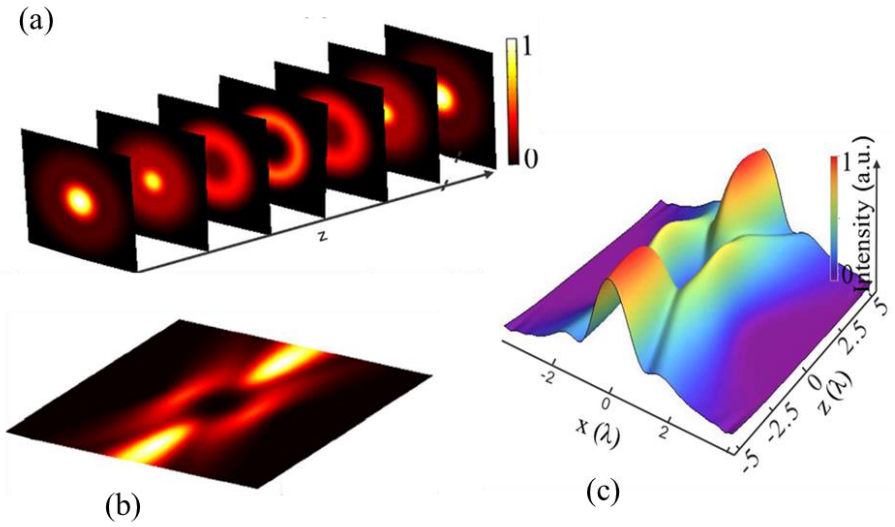


Fig. 1.5 (a) Beam propagation of a bottle beam. (b) Two-dimensional profile of the bottle beam with a dark core is completely enclosed by bright optical fields. (c) 3D profile of the bottle beam [36].

Going beyond the conventional optical vortices, the bottle beam has been collecting much attention in 3D trapping [37-42] and 3D guiding [43-46], in which more stable trapping and reliable manipulation of absorbing particles are allowed, thus, it may explore new advanced applications in optical, biological, and atmospheric sciences.

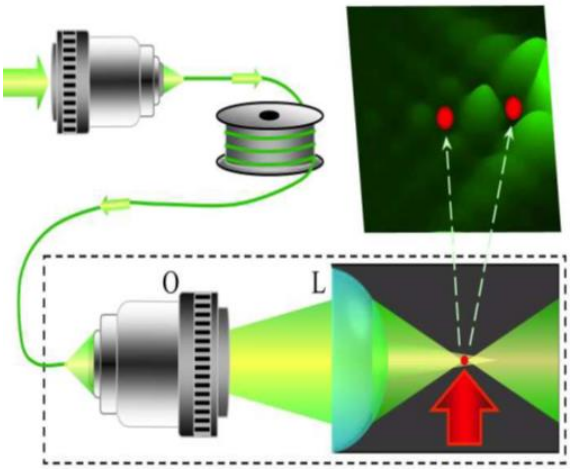


Fig. 1.6 3D atom trapping by employing the bottle beam.

Furthermore, the bottle beam will extend the super-resolution microscopes to 3D super-resolution microscopes, in which the fluorescence spot is far beyond the diffraction limit in all three dimensions [47-49].

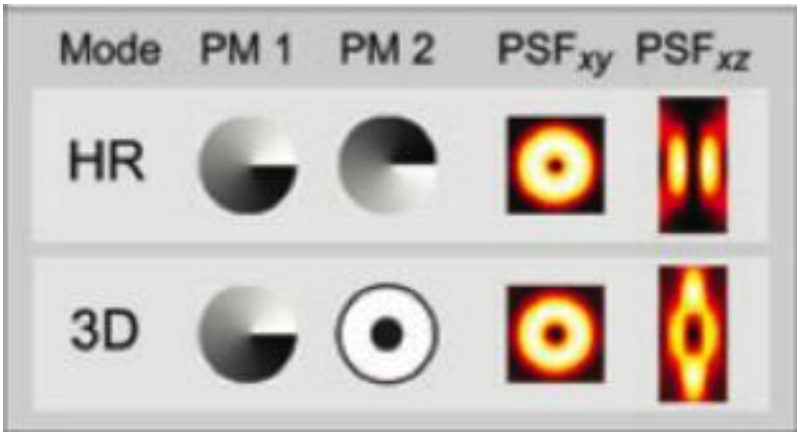


Fig. 1.7 3D 'super-resolution microscope' based on the bottle beam.

Also, the bottle beams can be used as optical cloaking in imaging systems [50,51]. As is

well known, the imaging system is based on the detection of the reflection, scattering or transmission of the optical field of the object. Therefore, if any object is hidden inside the 3D dark core of the bottle beam, shown in Fig. 1.8, it can inhibit the detection of the object.

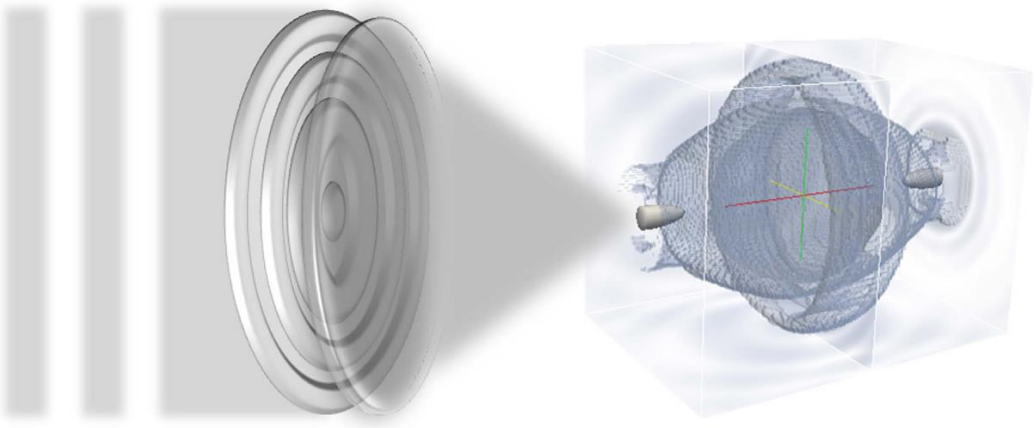

Fig. 1.8 Basic concept of optical cloaking [50].

Such applications certainly require the generation of bottle beams with a well-isolated 3D zero-intensity dark core, i.e., a high potential barrier.

## 1.4 Overview of the thesis

In this thesis, I have successfully demonstrated the direct generation of infrared/visible vortex beams and bottle beams from the diode-pumped solid-state lasers.

The thesis is organized as follows:

In chapter 1, I introduce the structured light beams, including the optical vortices and bottle beams, and their applications.

In chapter 2, I also review the eigen modes of the Helmholtz electro-magnetic equation with the paraxial approximation, including Hermite-Gaussian (HG) mode and LG modes. Also, the relationship between them is briefly discussed.

In chapter 3, several techniques to generate structured light beams, including the intra- and extra-cavity configurations, are addressed.

In chapter 4, the wavelength of the solid-state lasers is extended via nonlinear frequency conversion, including second harmonic generation and stimulated Raman Scattering.

In chapter 5, I report on a continuous-wave self-Raman Nd:$GdVO_4$ vortex laser based on the different Raman shifts of 382 $cm^{-1}$ and 882$cm^{-1}$ by shaping the pumping beam with the use of an axicon lens and a focusing lens. Selective generation of vortex beams at 1.108 μm or 1.173 μm, or both 1.108 μm and 1.173 μm, was achieved by merely aligning the output coupler of the laser cavity.

In chapter 6, I present the direct generation of red (640 nm) and orange (607 nm) vortex beams from a diode end-pumped $Pr^{3+}$:YLF laser with an off-axis pumping scheme. A numerical analysis, based on the coherent superposition of orthogonal HG modes with different amplitude and phase, is conducted.

In chapter 7, I first demonstrated the direct generation of bottle beams from a compact intracavity frequency-doubled Nd:$YVO_4$ laser with a nearly hemispherical cavity configuration.

Finally, I conclude my study and mention the prospective work of my thesis in chapter 7.

## 1.5 References


[1] L. A. Lugiato, C. Oldano, and L. M. Narducci, "Cooperative frequency locking and stationary spatial structures in lasers," JOSA B **5**(5), 879-888 (1988).

[2] P. Coullet, L. Gil, and F. Rocca, "Optical vortices," Opt. Commun. **73**, 403–408 (1989). 1622 (1989).

[3] M. Brambilla, F. Battipede, L. A. Lugiato, V. Penna, F. Prati, C. Tamm, and C. O. Weiss, "Transverse laser patterns. I. Phase singularity crystals," Phys. Rev. A **43**(9), 5090 (1991).

[4] M. Brambilla, L. A. Lugiato, V. Penna, F. Prati, C.Tamm, and C. O. Weiss, "Transverse laser patterns. II. Variational principle for pattern selection, spatial multistability, and laser hydrodynamics," Phys. Rev. A **43**, 5114–5120 (1991).

[5] L. A. Lugiato, G. L. Oppo, J. R. Tredicce, L. M. Narducci, and M. A. Pernigo, "Instabilities and spatial complexity in a laser," JOSA B **7**(6), 1019-1033 (1990).

[6] K. Staliunas, and V. J. Sanchez-Morcillo, "Transverse patterns in nonlinear optical resonators," Springer Science & Business Media, 183 (2003).

[7] C. Tamm, "Frequency locking of two transverse optical modes of a laser," Phys. Rev. A **38**(11), 5960 (1988).

[8] L. C. Crasovan, B. A. Malomed, and D. Mihalache, "Stable vortex solitons in the two-dimensional Ginzburg–Landau equation," Phys. Rev. E **63**, 016605 (2000).
[9] N. N. Rosanov, S. V. Fedorov, and A. N. Shatsev, "Curvilinear motion of multivortex laser-soliton complexes with strong and weak coupling," Phys. Rev. Lett. **95**, 053903 (2005).
[10] L. Allen, M. W. Beijersbergen, R. J. C. Spreeuw, and J. P. Woerdman, "Orbital angular momentum of light and the transformation of Laguerre–Gaussian laser modes," Phys. Rev. A **45**, 8185–8189 (1992).
[11] V. Y. Bazhenov, M. S. Soskin, and M. V. Vasnetsov, "Screw dislocations in light wavefronts," J. Mod. Opt. **39**, 985–990 (1992).
[12] D. Mihalache, D. Mazilu, V. Skarka, B. A. Malomed, H. Leblond, N. B. Aleksić, and F. Lederer, "Stable topological modes in two-dimensional Ginzburg-Landau models with trapping potentials," Phys. Rev. A **82**, 023813 (2010).
[13] S. Barland, E. Caboche, P. Genevet, X. Hachair, M. Giudici, F. Pedaci, and J. R. Tredicce, "Observation of "true" optical vortices in a laser system," In Nonlinear Photonics and Novel Optical Phenomena (pp. 195-205) Springer, New York, (2012).
[14] J. Arlt and M. J. Padgett, "Generation of a beam with a dark focus surrounded by regions of higher intensity: the optical bottle beam," Opt. Lett. **25**, 191-193 (2000).
[15] M. Padgett, J. Courtial, L. Allen, "Light's orbital angular momentum," Phys. Today **57**, 35-40 (2004).
[16] A. M. Yao, M. J. Padgett, "Orbital angular momentum: origins, behavior and applications," Adv. Opt. Photon. **3**, 161-204 (2011).
[17] M. P. J. Lavery, F. C. Speirits, S. M. Barnett, and M. J. Padgett, "Detection of a spining object using light's orbital anglar momentum," Science **341** (6145), 537-540 (2013).
[18] M. J. Padgett, "Orbital angular momentum 25 years on," Opt. Express **25**, 11265-11274 (2017).
[19] H. Rubinsztein-Dunlop, A. Forbes, M. V. Berry, M. R. Dennis, D. L. Andrews, M. Mansuripur, C. Denz, C. Alpmann, P. Banzer, T. Bauer, E. Karimi, L. Marrucci, M. J. Padgett, M. Ritsch-Marte, N. M. Litchinitser, N. P. Bigelow, C.Rosales-Guzmán, A. Belmonte, J. P. Torres, T. W. Neely, M. Baker, R. Gordon, A. B. Stilgoe, J. Romero, A. G.White, R. Fickler, A. E. Willner, G. Xie, B. McMorran, and A. M. Weiner, "Roadmap on structured light," J. Opt. **19** (1), 013001 (2017).

[20] K. Toyoda, K. Miyamoto, N. Aoki, R. Morita, T. Omatsu, "Using optical vortex to control the chirality of twisted metal nanostructures," Nano Lett. **12**, 3645-3649 (2012).

[21] S. Syubaev, A. Zhizhchenko, A. Kuchmizhak, A. Porfirev, E. Pustovalov, O. Vitrik, Yu. Kulchin, S. Khonina, and S. Kudryashov, "Direct laser printing of chiral plasmonic nanojets by vortex beams," Opt. Express **25**, 10214-10223 (2017).

[22] M. G. Rahimian, F. Bouchard, H. Al-Khazraji, E. Karimi, P. B Corkum, and V. R Bhardwaj, "Polarization dependent nanostructuring of silicon with femtosecond vortex pulse," APL Photonics **2**, 086104 (2017).

[23] S. Kawagoe, R. Nakamura, R. Tasaki, H. Oshima, M. Higashihata, D. Nakamura, T. Omatsu, "Microfabrication of Au film using optical vortex beam," J. Laser Micro Nanoeng. **14**, 31-34 (2019).

[24] S. Syubaev, A. Zhizhchenko, O. Vitrik, A. Porfirev, S. Fomchenkov, S. Khonina, S. Kudryashov, and A. Kuchmizhak, "Chirality of laser-printed plasmonic nanoneedles tunable by tailoring spiral-shape pulses," Appl. Surf. Sci. **470**, 526-534 (2019).

[25] J. Lee, Y. Arita, S. Toyoshima, K. Miyamoto, P. Panagiotopoulos, E. M. Wright, K. Dholakia, T. Omatsu, "Photopolymerization with light fields possessing orbital angular momentum: generation of helical microfibers," ACS Photonics **5**, 4156-4163 (2018).

[26] T. Watanabe, Y. Iketaki, T. Omatsu, K. Yamamoto, M. Sakai, M. Fujii, "Two-point-separation in super-resolution fluorescence microscope based on up-conversion fluorescence depletion technique," Opt. Express **11**, 3271-3276 (2003).

[27] J. Keller, A. Schönle, and S. W. Hell, "Efficient fluorescence inhibition patterns for RESOLFT microscopy," Opt. Express **15**, 3361-3371 (2007).

[28] M. Kamper, H. Ta, N. A. Jensen, S. W. Hell, S. Jakobs, "Near-infrared sted nanoscopy with an engineered bacterial phytochrome," Nat. Commun. **9**, 1-7 (2018).

[29] J. Leach, B. Jack, J. Romero, A. K. Jha, A. M. Yao, S. Franke-Arnold, D. G. Ireland, R. W. Boyd, S. M. Barnett, M. J. Padgett, "Quantum correlations in optical angle–orbital angular momentum variables," Science **329**, 662-665 (2010).

[30] V. D. Ambrosio, E. Nagali, S. P. Walborn, L. Aolita, S. Slussarenko, L. Marrucci, and F. Sciarrino, "Complete experimental toolbox for alignment-free quantum communication," Nat. Commun. **3** (1), 961 (2012).

[31] N. Bozinovic, Y. Yue, Y. Ren, M. Tur, P. Kristensen, H. Huang, A. E. Willner, S. Ramachandran, "Terabit-scale orbital angular momentum mode division multiplexing in fibers," Science **340**, 1545-1548 (2013).

[32] Y. Yan, G. Xie, M. P. Lavery, H. Huang, N. Ahmed, C. Bao, Y. Ren, Y. Cao, L. Li, Z. Zhao, A. F. Molisch, M. Tur, M. J. Padgett, A. E. Willner, "High-capacity millimetre-wave communications with orbital angular momentum multiplexing," Nat. Commun. **5**, 1-9 (2014).

[33] A. E. Willner, H. Huang, Y. Yan, Y. Ren, N. Ahmed, G. Xie, C. Bao, L. Li, Y. Cao, Z. Zhao, J. Wang, M. P. J. Lavery, M. Tur, S. Ramachandran, A. F. Molisch, N. Ashrafi, and S. Ashrafi, "Optical communications using orbital angular momentum beams," Adv. Opt. Photonics **7** (1), 66 (2015).

[34] J. Wang, "Advances in communications using optical vortices," Photon. Res. **4**, B14-B28 (2016).

[35] L. Zhu, A. Wang, S. Chen, J. Liu, J. Wang, "Orbital angular momentum mode multiplexed transmission in heterogeneous few-mode and multi-mode fiber network," Opt. Lett. **43** (8), 1894-1897 (2018).

[36] G. Lei, W. Liu, Q. Zhao, Y. Ren, X. Qiu, M. Zhong and Y. Li, "Controllable light capsules employing modified Bessel-Gauss beams," Sci. Rep. **6**, 29001 (2016).

[37] R. Ozeri, L. Khaykovich, and N. Davidson, "Long spin relaxation times in a single-beam blue-detuned optical trap," Phys. Rev. A **59**(3), 1750-1753 (1999).

[38] L. Isenhower, W. Williams, A. Dally, and M. Saffman, "Atom trapping in an interferometrically generated bottle beam trap," Opt. Lett. **34**, 1159 (2009).

[39] R. Grimm, M. Weidemuller, and Y. B. Ovchinnikov, "Optical dipole traps for neutral atoms," Adv. At. Mol. Opt. Phys. **42**, 95-170 (2000).

[40] P. Xu, X. He, J. Wang, and M. Zhan, "Trapping a single atom in a blue detuned optical bottle beam trap," Opt. Lett. **35**(21), 2164-2166 (2010).

[41] T. Puppe, I. Schuster, A. Grothe, A. Kubanek, K. Murr, P. W. H. Pinkse, and G. Rempe, "Trapping and observing single atoms in a blue-detuned intracavity dipole trap," Phys. Rev. L, **99**(1), 013002 (2007).

[42] G. Li, S. Zhang, L. Isenhower, K. Maller, and M. Saffman, "Crossed vortex bottle beam trap for single-atom qubits," Opt. Lett. **37**, 851-853 (2012)

[43] V. G. Shvedov, C. Hnatovsky, A. V. Rode, and W. Krolikowski, "Robust trapping and manipulation of airborne particles with a bottle beam," Opt. Express **19**, 17350-17356 (2011).

[44] V. G. Shvedov, A. S. Desyatnikov, A. V. Rode, W. Krolikowski, and Y. S. Kivshar, "Optical guiding of absorbing nanoclusters in air," Opt. Express **35**(13), 2164-2166 (2010).
[45] B. P. S. Ahluwalia, X. C. Yuan, and S. H. Tao, "Transfer of 'pure' on-axis spin angular momentum to the absorptive particle using self-imaged bottle beam optical tweezers system," Opt. Express **12**(21), 5172-5177 (2004).
[46] P. Zhang, Z. Zhang, J. Prakash, S. Huang, D. Hernandez, M. Salazar, D. N. Christodoulides, and Z. Chen "Trapping and transporting aerosols with a single optical bottle beam generated by moiré techniques," Opt. Lett. **36**(8), 1491-1493 (2011).
[47] Y. Iketaki, H. Kumagai, K. Jahn, and N. Bokor, "Creation of a three-dimensional spherical fluorescence spot for super-resolution microscopy using a two-color annular hybrid wave plate," Opt. Lett. **40**(6), 1057-1060 (2015).
[48] D. Wildanger, R. Medda, L. Kastrup, and S. W. Hell, "A compact STED microscope providing 3D nanoscale resolution," J. Microsc. **236**(1), 35-43 (2009).
[49] J. Keller, A. Schönle, and S. W. Hell, "Efficient fluorescence inhibition patterns for RESOLFT microscopy," Opt. Express **15**, 3361-3371 (2007).
[50] H. Wang, J. Lin, D. Zhang, Y. Wang, M. Gu, H. P. Urbach, F. Gan, and S. Zhuang, "Creation of an anti-imaging system using binary optics," Sci. Rep. **6**(1), 33064 (2016).
[51] T. Čižmár1 and K. Dholakia, "Exploiting multimode waveguides for pure fibre-based imaging," Nature Commun. **3**, 1027 (2012).

# 2 Overview of higher-order transverse modes

In this chapter, the detailed expression of the propagation of light is obtained by employing Maxwell's equations to derive the electro-magnetic wave equations.

## 2.1 Paraxial wave equation

We consider a laser cavity formed of plane mirrors at $z = 0$ and $z = L$. The electro-magnetic interaction in the cavity can be expressed by the following Maxwell's equations

$$\nabla \times \mathbf{E} = -\frac{\partial \boldsymbol{B}}{\partial t} \tag{2.1.1}$$

$$\nabla \times \mathbf{H} = \mathbf{J}_f + \frac{\partial \boldsymbol{D}}{\partial t} \tag{2.1.2}$$

$$\nabla \cdot \mathbf{D} = \rho_f \tag{2.1.3}$$

$$\nabla \cdot \mathbf{B} = 0 \tag{2.1.4}$$

, where $\rho_f$ is the free charge density, and $\mathbf{J}_f$ is the free current density; **E**, **D**, **B**, and **H** are the electric field, electric flux density, magnetic flux density, and magnetic field, respectively. In the cavity formed of dielectric materials, we can assume

$$\rho_f = 0 \tag{2.1.5}$$

$$\mathbf{B} = \mu_0 \mathbf{H} \tag{2.1.6}$$

$$\mathbf{D} = \varepsilon_0 \mathbf{E} + \mathbf{P} \tag{2.1.7}$$

$$\mathbf{J}_f = \sigma \mathbf{E} \tag{2.1.8}$$

where **P** is the polarization, $\sigma$ is the conductivity, and $\varepsilon_0$ and $\mu_0$ are the dielectric permittivity and magnetic permeability in free space.

Using $\nabla \times \nabla \times \mathbf{E} = \nabla(\nabla \cdot \mathbf{E}) - \nabla^2 \boldsymbol{E}$, where $\nabla^2 = \partial_x^2 + \partial_y^2 + \partial_z^2$ is the Laplacian.

If taking the rotation of Eq.(1.1), we can obtain

$$\nabla^2 \boldsymbol{E} - \epsilon_0 \mu_0 \frac{\partial^2}{\partial t^2} \boldsymbol{E} = 0 \tag{2.1.9}$$

Eq.(2.1.9) is termed the electro-magnetic wave equation. By substituting a wave function, given by $E(r,\mathrm{t}) = E(\mathrm{r})\exp(i\omega t)$, into Eq.(1.9), the Helmholtz equation is given as

$$(\nabla^2 + k^2)\boldsymbol{E} = 0 \tag{2.1.10}$$

where $-\epsilon_0\mu_0 = k^2$.

The general form of the field wave is given by

$$\boldsymbol{E}(\boldsymbol{r},\mathrm{t}) = \hat{e}u(\boldsymbol{r},t)\exp[i(kz-\omega t)] + c.c \tag{2.1.11}$$

In general, it can be assumed that the magnitude of the electric field is slowly varying through the beam propagation (*i.e.* slowly varying envelope approximation),

$$\frac{\partial^2}{\partial z^2}u \ll 2k\frac{\partial u}{\partial z} \tag{2.1.12}$$

, thus, we obtain the following equation given by,

$$\frac{\partial^2 u}{\partial x^2} + \frac{\partial^2 u}{\partial y^2} - 2ik\frac{\partial u}{\partial z} = 0 \tag{2.1.13}$$

Equation (2.1.13), called Helmholtz electro-magnetic wave equation with the paraxial approximation, can be solved in each of the Cartesian and the cylindrical coordinate systems. Its eigen modes are called HG beam and Laguerre-Gaussian beam, respectively. The detailed solutions will be shown in follows.

## 2.2 Gaussian modes

The complete expression for the fundamental or lowest-order $\mathrm{TEM}_{0,0}$ mode (called Gaussian mode [1,2]) is given by

$$\mathrm{E}(\mathrm{x},\mathrm{y},\mathrm{z}) = E_0\frac{\omega_0}{\omega_{(z)}}\exp\left[-\frac{\rho^2}{\omega(z)^2}\right]\exp\left[i\xi(z)\right]\exp\left[-ikz\right]\exp(-\frac{ik\rho^2}{2R(z)}), \tag{2.2.1}$$

where

$$\rho = \sqrt{x^2 + y^2} \ , \tag{2.2.2}$$

$$\omega(z) = \omega_0 \sqrt{1 + \left(\frac{z}{z_R}\right)^2} \ , \tag{2.2.3}$$

$$R(z) = z\left[1 + \left(\frac{z_R}{z}\right)^2\right] \tag{2.2.4}$$

$$\omega_0 = z\sqrt{\frac{\lambda z_R}{\pi}} \ , \tag{2.2.5}$$

$$\xi(z) = \arctan\left(\frac{z}{z_R}\right) . \tag{2.2.6}$$

In particular, the amplitude of the fundamental field at z = 0, can be described by

$$\mathrm{E(x,y)} = E_0 \frac{\omega_0}{\omega_{(z)}} \exp\left(-\frac{\rho^2}{\omega_0^2}\right)$$

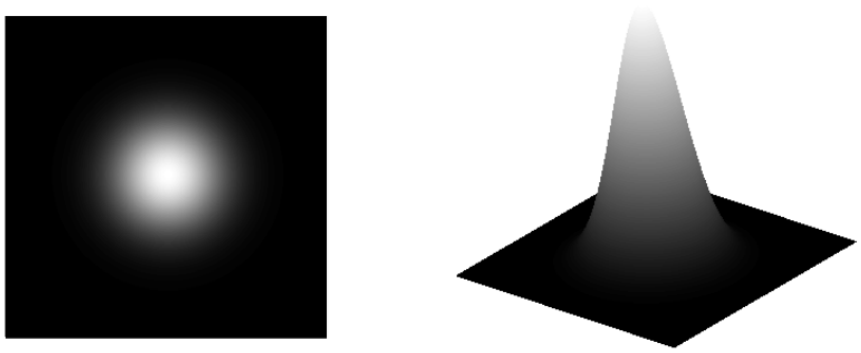

Fig. 2.1 Spatial form of Gaussian beam.

## 2.3 Higher-order modes

Electric fields oscillating inside the resonator, called the eigen modes of the resonator, are given by three families, such as Hermite-Gaussian (HG) modes with rectangular symmetry, LG modes with cylindrical symmetry, and Ince-Gaussian (IG) modes for elliptical symmetry. This thesis primarily focuses on HG and LG modes.

### 2.3.1 Hermite-Gaussian modes

The HG modes are a family of paraxial solutions to the wave equation in Cartesian coordinates. Their mathematical expression is given by the product of a Gaussian function and the Hermite polynomial $HG_{nm}(x)$ as follows [3]:

$$HG_{nm}(x,y,z) = \frac{1}{\omega(z)}\sqrt{\frac{2^{(1-n-m)}}{\pi n!\, m!}}H_n\left(\frac{\sqrt{x}}{\omega(z)}\right)H_m\left(\frac{\sqrt{y}}{\omega(z)}\right)$$

$$\exp\left[i(n+m+1)\xi(z)\right]\exp\left[-\left(\frac{\rho}{\omega(z)}\right)^2\right]\exp\left[-\frac{ik\rho^2}{2R(z)}\right]\exp\left[-ikz\right], \qquad (2.3.1)$$

where $n$ and $m$ are the positive integers and $\lambda$ is the wavelength, respectively.

The above equation represents a paraboloidal wave with a radius of curvature $R(z)$, and a second moment beam size of $\omega(z)$. $\omega(z)$ exhibits its minimum value $\omega_0$ at $z = 0$, called the beam waist. The term $z_R$ is the Rayleigh range, in which the beam remains well collimated with nearly planar wavefronts. The parameter $\xi(z)$, known as the Gouy phase, indicates that the wavefront acquires an additional phase shift of half a wavelength compared to an ideal plane wave, in passing through the waist. Figure 2.2 shows the intensity profiles of several HG modes.

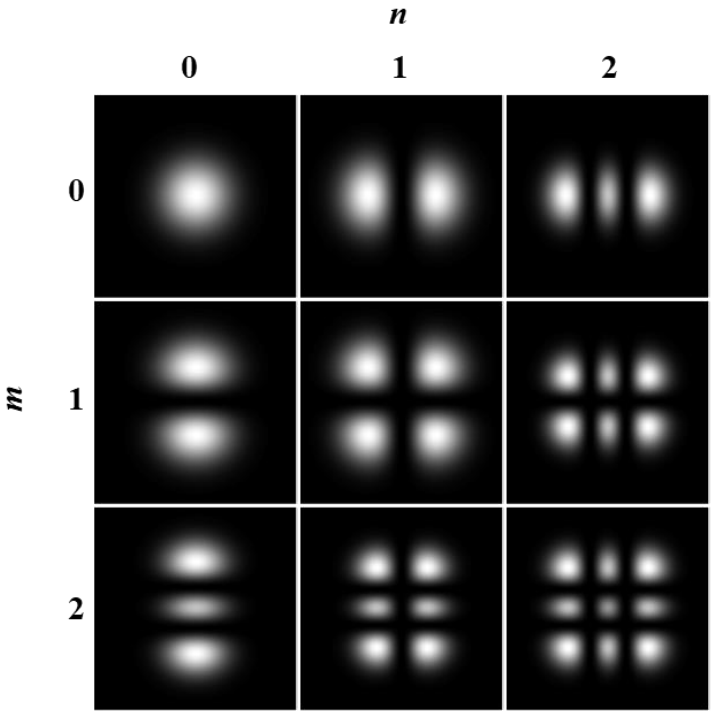


Fig. 2.2 Spatial forms of various HG modes.

## 2.3.2 Laguerre-Gaussian modes

LG beams are eigen modes of the paraxial Helmholtz equation at cylindrical coordinates. Their mathematical representation is given in terms of a Gaussian function and the Laguerre polynomial $LG_{p,\ell}(x)$ as,

$$LG_p^{\ell}(\rho,\varphi,z) = \frac{\omega_0}{\omega(z)}\sqrt{\frac{2p!}{\pi(|\ell|+p)!}}\left(\frac{\sqrt{2}\rho}{\omega(z)}\right)^{|\ell|} L_p^{\ell}\left[2\left(\frac{\rho}{\omega(z)}\right)^2\right]$$
$$\exp[i(2p+|\ell|+1)\xi(z)]\exp\left[-\left(\frac{\rho}{\omega(z)}\right)^2\right]\exp\left[-\frac{ik\rho^2}{2R(z)}\right]\exp[-i\ell\varphi], \qquad (2.3.2)$$

where $p$ = 0, 1, 2…is the radial index, and $\ell$ =…,-2,-1,0,1,2,… is the azimuthal index, $\rho$ is the radial coordinate, and $\varphi$ is the angle around the optical axis of the laser.

The Laguerre polynomials can be found in the mathematical handbooks [4]. For low orders $p$=0~3, they are

$$L_0^{\ell}(x) = 1\,, \qquad (2.3.7)$$
$$L_1^{\ell}(x) = \ell + 1 - x\,, \qquad (2.3.8)$$
$$L_2^{\ell}(x) = 0.5(\ell+1)(\ell+2) - (\ell+2)x + 0.5x^2\,, \qquad (2.3.9)$$
$$L_3^{\ell}(x) = \frac{(\ell+1)(\ell+2)(\ell+3)}{6} - 0.5(\ell+2)(\ell+3)x + 0.5(\ell+3)x^2 - \frac{x^3}{6}\,. \qquad (2.3.10)$$

Figure 2.3 shows the intensity spatial forms of several LG beams with different indices of $p$ and $\ell$.

In particular, LG modes with zero azimuthal and non-zero radial indices, i.e., $p \neq 0$, and $\ell$ = 0, called radial LG modes. These radial LG modes have significant to generate bottle beams. Besides, when azimuthal index $\ell$ is not equal to zero, with an azimuthal phase term $\exp[i\ell\varphi]$, called vortex modes.

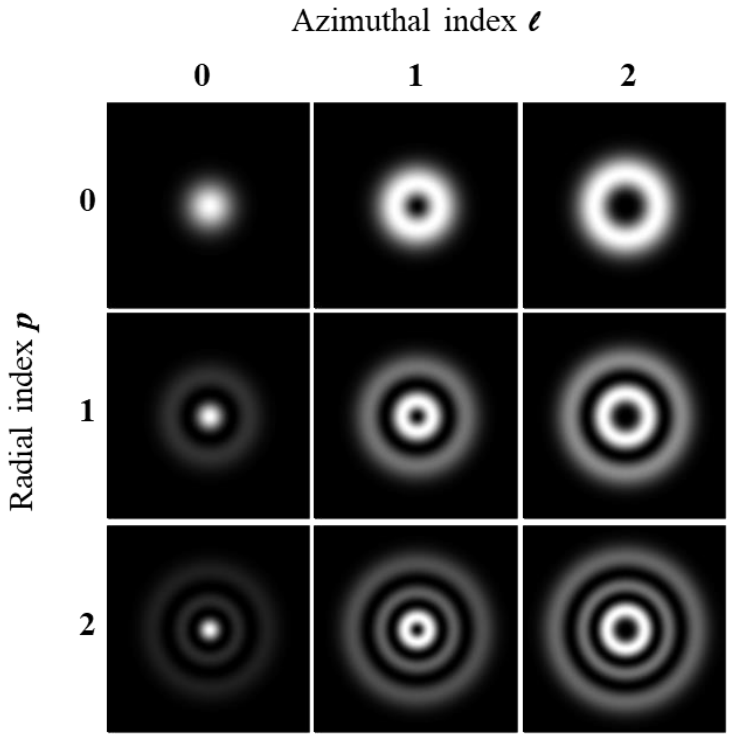


Fig. 2.3 Spatial forms of LG modes with different indices.

## 2.3.3 Mode conversion between the HG and LG modes

The HG modes can be converted into appropriate LG modes by employing a cylindrical-lens mode converter [5], shown in Fig. 2.4.

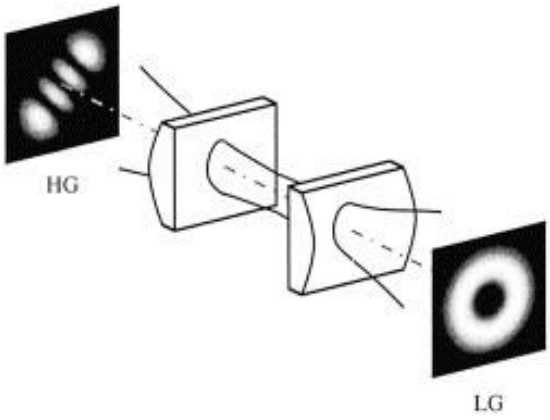


Fig. 2.4 Cylindrical-lens HG-LG mode converter.

The general formula between individual $HG_{n,m}$ and LG $_{p,\ell}$ modes can be established. The indices $\ell$ and $p$ of the LG mode resulting from mode conversion of an HG mode with the indices $n$ and $m$ are given by

$$\ell\,(n, m) = n - m, \quad p\,(n, m) = \min(n, m). \tag{2.3.11}$$

It is worth noting that $\ell$ can exhibit negative values. Thus, the formula between HG and LG modes is defined as

$$N = n + m = 2p + |\ell|. \tag{2.3.12}$$

Table 1 lists all corresponding pairs of mode indices ( $n$, $m$ ) and ($\ell$, p) for mode orders $N$ =1, 2, 3. The cylindrical lens mode converter also enables any LG mode with $\ell$ and $p$ to transform into its corresponding HG mode with $n$ and $m$. The corresponding $n$ and $m$ can be expressed in the form

$$n = (N + \ell)/2,\ m = (N - \ell)/2, \tag{2.3.13}$$

, where $N$ is the mode order of the incident LG mode (which is also the same as that of the output HG mode).

Table 1

All corresponding pairs of mode indices ($n$, $m$) and ($\ell$, $p$) for mode orders $N$ = 0, 1, 2.

| N | ($n$, $m$) | ($\ell$, $p$) |
|---|---|---|
| 0 | (0,0) | (0,0) |
| 1 | (1,0) | (1,0) |
| | (0,1) | (-1,0) |
| 2 | (2,0) | (2,0) |
| | (1,1) | (0,1) |
| | (0,2) | (-2,0) |

## 2.4 References

[1] H. Kogelnik and T. Li, “Laser Beams and Resonators,” Appl. Opt. 5(10), 1550-1567 (1966).

[2] S. Saghafi, and C. J. R. Sheppard, “Near field and far field of elegant Hermite-Gaussian and Laguerre-Gaussian modes” J. Mod. Opt. 45(10), 1999-2009 (1998).

[3] N. Hodgson, and H. Weber, Laser Resonators and Beam Propagation: Fundamentals, Advanced Concepts, Applications (Vol. 108). Springer. (2005).

[4] M. Abramowitz, and I. A. Stegun, Handbook of Mathematical Functions (Dover, New York, 1970).

[5] A. T. O'Neil, and J. Courtial, “Mode transformations in terms of the constituent Hermite–Gaussian or Laguerre–Gaussian modes and the variable-phase mode converter,” Opt. Commun. **181**(1-3), 35-45 (2000).

# 3 Methods to generate structured light beams

## 3.1 Methods to generate optical vortices

Use of some optical phase modulation elements, such as spiral phase plates and spatial light modulators, is the most commonly used to produce optical vortex beams.

Direct generation of LG modes as an eigen mode from a laser cavity is an alternative way to produce high-quality vortex beams. Many remarkable methods, based on a ring-shaped beam pumping, a spot-defect mirror, an intra-cavity phase modulating element, and an off-axis pumping configuration, have been proposed.

### 3.1.1 Extra-cavity configuration

There are several methods to generate the optical vortices outside a laser cavity, *i.e.* extra-cavity configuration. A spiral phase plate [1–5], formed of a glass plate with a refractive index $n$ and azimuthally varying thickness, is most commonly used, thereby yielding the OAM mode with a helical wavefront. It is usually designed for only specific wavelengths, and it also prevents the management of high optical powers.

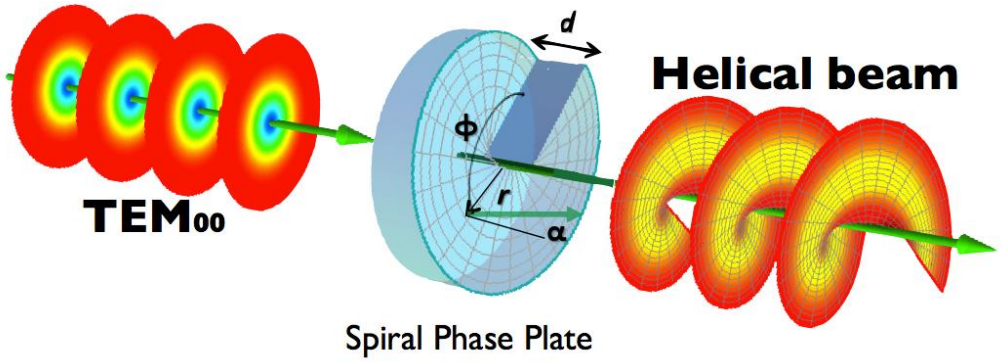


Fig. 3.1 Spiral phase plate for generating an optical vortex beam from an incident Gaussian beam.

A mode converter [6-10] formed of two cylindrical lenses with a focal length $f$ and an interval of $\sqrt{2}f$ ($\pi/2$ converter) or $2f$ ($\pi$ converter) is alternative. Such mode converter

is very sensitive to alignment, however, it enables the perfect mode conversion from an HG mode to its corresponding LG mode.

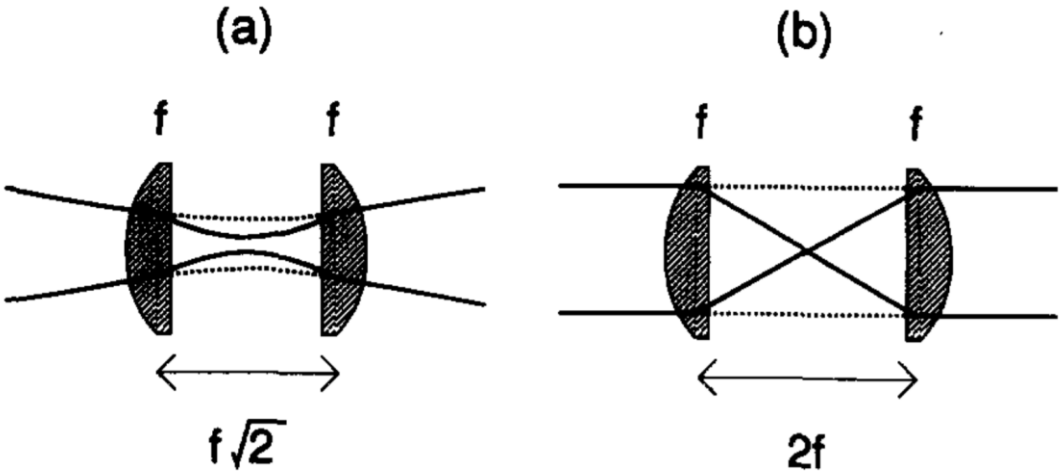


Fig. 3.2 HG-LG mode converters consisting of two cylindrical lenses with a focal length *f*. (a) $\pi/2$ phase shift mode converter and (b) $\pi$ phase shift mode converter.

A hologram with a linear phase ramp and an azimuthal $\ell$-fold phase expressed as modulo $2\pi$ also produces efficiently the optical vortex as a 1st order diffracted light as shown in Fig. 3.3.

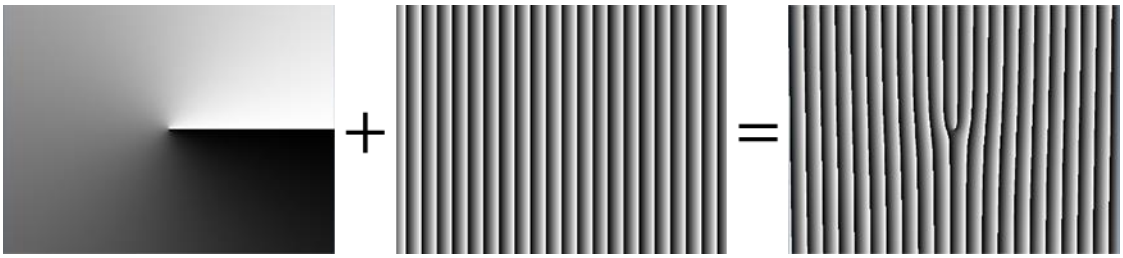

Fig. 3.3 Computer-generated hologram formed by the sum of a desired phase element (left) and a linear phase ramp (middle). It exhibits a forked diffraction grating (right), thereby producing a first order optical vortex mode with $\ell$ =1.

A spatial light modulator (SLM) [15-20], consisting of electrically-addressed 2-dimensional liquid crystal array, also allows us to produce a variety of structured light beams with arbitrary phase and amplitude, including optical vortices with any topological charges

and their superpositions. However, these holographic elements frequently impact the power scaling of the optical system [11-14] owing to their relatively high diffraction losses and low optical damage thresholds.

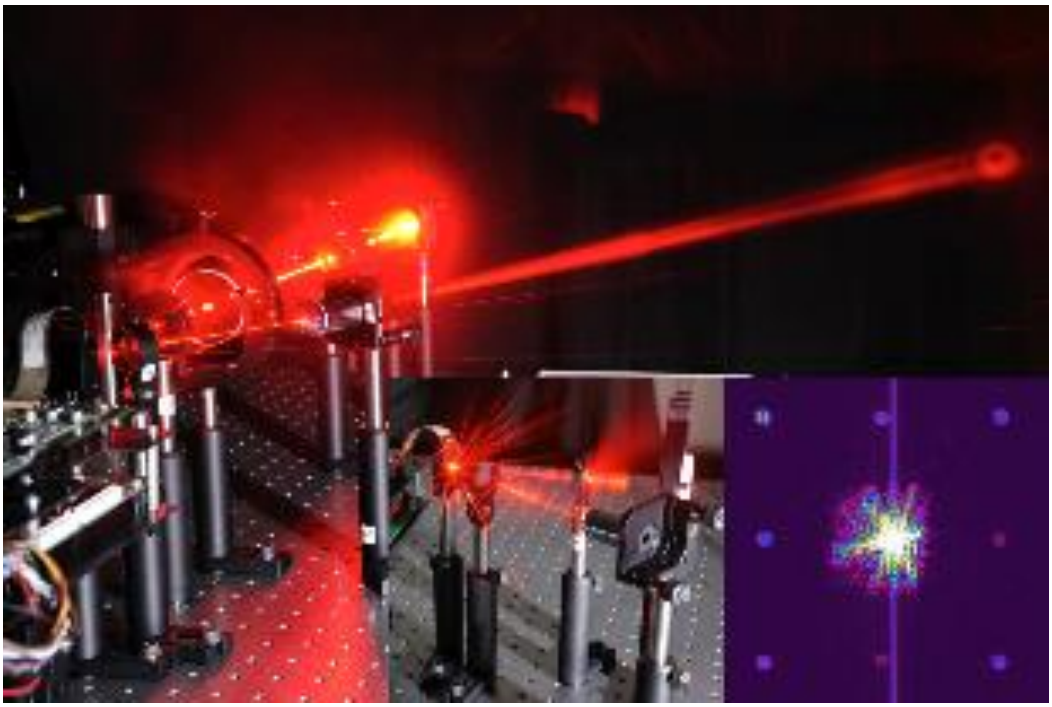

Fig. 3.4 Spatial light modulator (SLM) used for beam shaping to create a light field with orbital angular momentum. The insets show the diffractions owing to the SLM pixels.

Thus, these extra-cavity methods are accompanied owing to their limitation of power managements, and it is difficult to achieve high power vortex mode with high quality.

## 3.1.2 Intra-cavity configuration

Several laser cavities also allow the preferential oscillation of $LG_{0\ell}$ mode without any Gaussian mode, thereby yielding high quality optical vortex beams as an eigen mode.

For instance, the laser cavity with a doughnut-shaped pumping configuration has been utilized to produce efficiently LG modes in many laser systems with the aid of thermal lensing effects or intra-cavity mode selection elements [21-27].

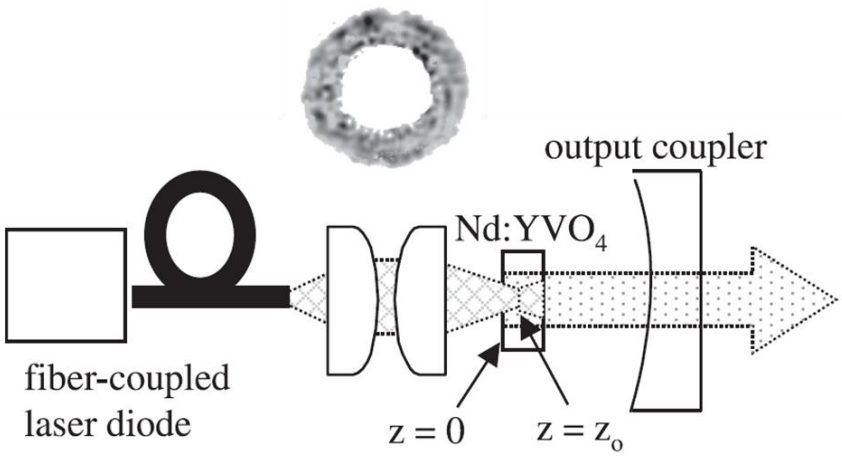


Fig. 3.5 Experimental setup for the $LG_{0\ell}$ mode generated from $Nd:YVO_4$ laser with a doughnut-shaped pumping configuration.

$LG_{0\ell}$ beams also can be directly obtained from the laser cavity with a spot-defect cavity mirror [28-32], *i.e.* engineered damage spots on resonator mirrors. In fact, the spot-defect mirror requires accurate mode matching between the lowest order Gaussian mode and the defect spot, however, it can break easily the symmetry of the laser resonator, thereby enabling us to operate at a preferential $LG_{0\ell}$ mode. A schematic diagram of an experimental setup of this technique is shown in Fig. 3.5.

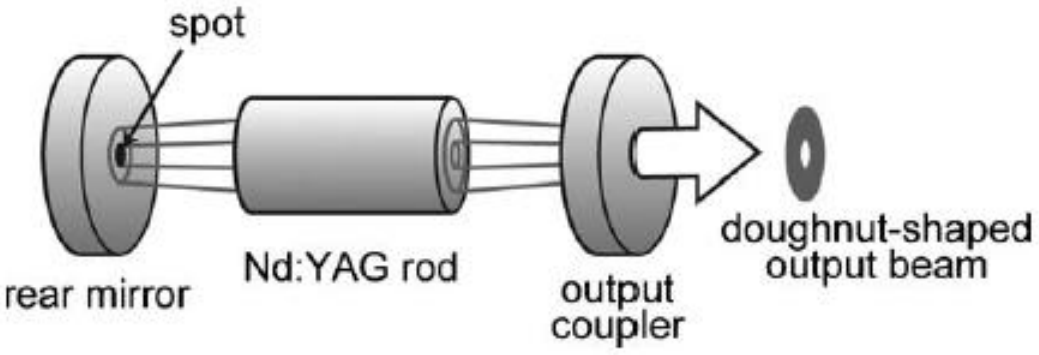


Fig. 3.6 Schematic of a Nd:YAG laser with a spot-defect cavity mirror. This system produces efficiently $LG_{0\ell}$ modes.

Digital lasers [33-36] consist of an electrically addressed reflective phase-only SLM as an intra-cavity digitally addressed holographic mirror. They allow the direct generation of a myriad of laser modes by dynamically changing a computer-generated hologram.

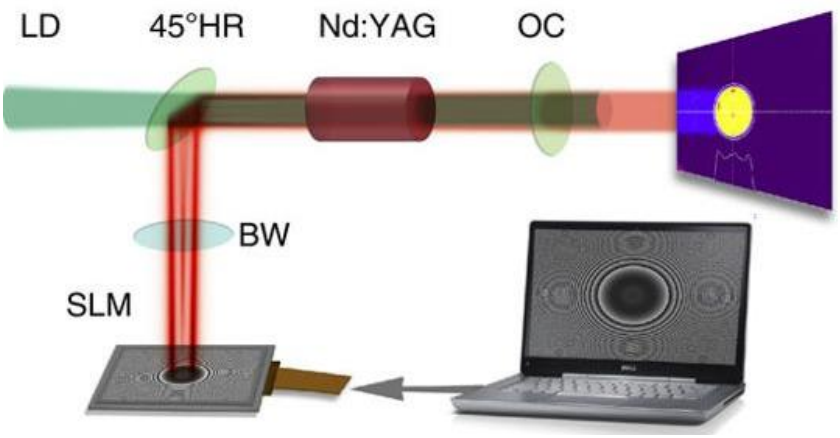


Fig. 3.7 Digital laser based on intra-cavity phase-only SLM.

## 3.2 Methods to generate bottle beams

To date, several techniques for generating bottle beams have been proposed. For instance, radial-order LG modes with zero azimuthal index and non-zero radial index are produced by the use of computer-generated holograms, and they then interfere destructively at their beam waists to shape the bottle beam [37-41]. Such digital holograms can also be used to design preferential bottle beams with arbitrary potential barriers, though rather complex calculations are required.

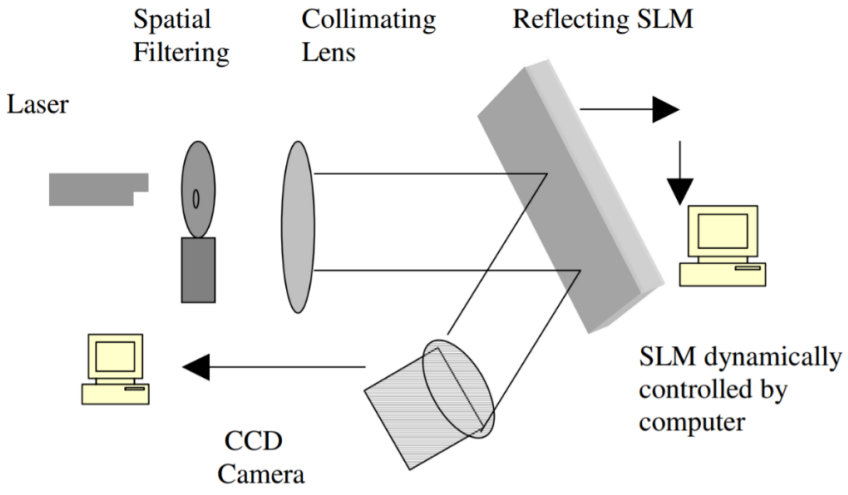


Fig. 3.8 Experimental setup for generating bottle beams by computer-generated holograms.

The most straightforward way to generate a bottle beam is to use an axicon lens combined with a focus lens [41-45], as shown in Fig. 3.9. A plane wave is transformed by an axicon

lens to be a Bessel beam within a gray region. Subsequently, a focusing lens further transforms the Bessel beam to be a bottle beam with an on-axis dark core surrounded by the bright light fields within the range of Δz. However, in general, the generated bottle beam exhibits rather large dark core with low potential barrier.

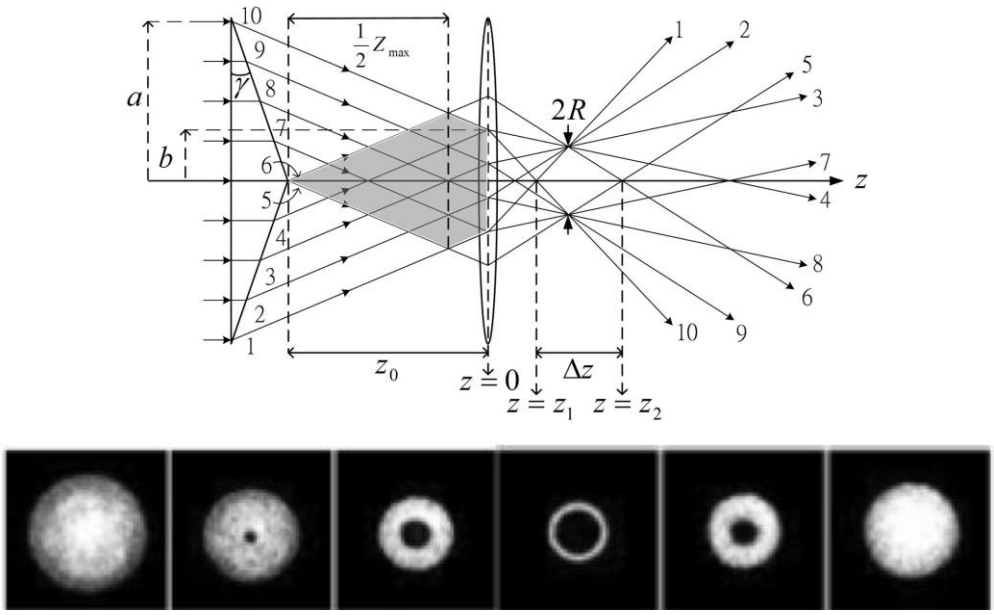


Fig. 3.9 (a) Schematic of bottle beam generation by employing an axicon lens and a focusing lens. (b) Beam propagation of the generated bottle beam.

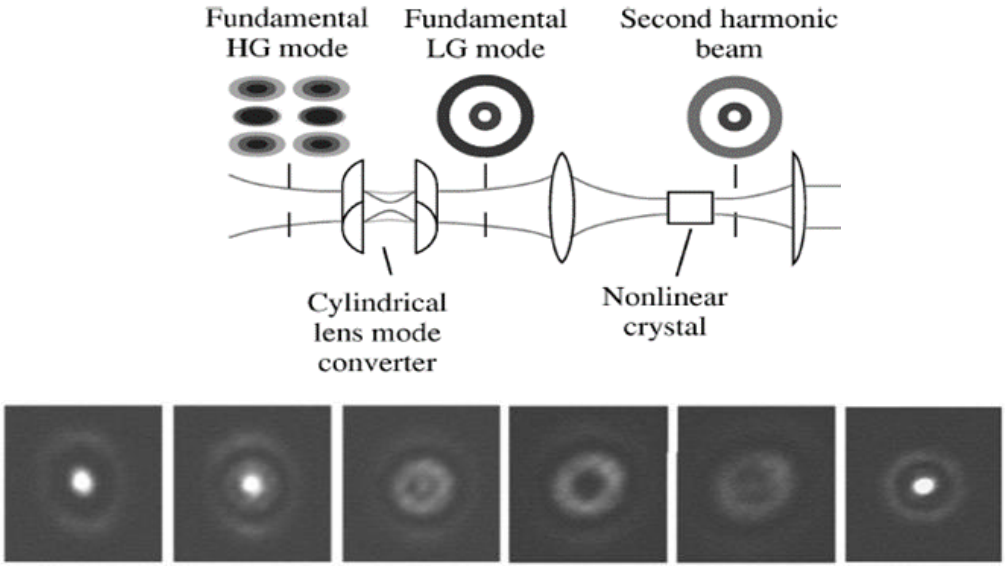


Fig. 3.10 (a) Schematic of bottle beam generation from an extra-cavity SHG configuration. (b) Beam propagation of the generated bottle beam at different longitudinal positions.

Frequency doubled radial LG mode also exhibits physical properties of bottle beam [46] formed of the coherent superposition of radial LG modes, however, its potential barrier is relatively low.

A degenerate cavity configuration [47,48] with an appropriate intra-cavity aperture forces the lasers to operate at only a Gaussian and a degenerate transverse mode, thereby yielding the bottle beam formed of the superposition of the Gaussian and degenerate transverse modes. However, the generated bottle beams exhibit rather low potential barriers.

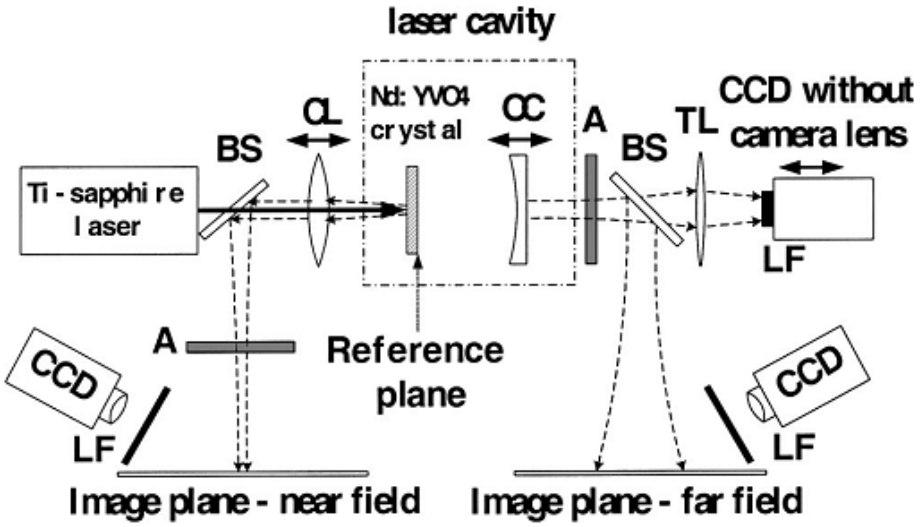


Fig. 3.11 Generation of in-phase radial-order LG modes by employing a near degenerate cavity.

## 3.3 References

[1] V.V. Kotlyar, A.A. Almazov, S.N. Khonina, V.A. Soifer, H. Elfstrom, J. Turnen, "Generation of phase singularity through diffracting a plane or Gaussian beam by a spiral phase plate," J. Opt. Soc. A. **22**, 849–861 (2005).

[2] M. W. Beijersbergen, R. P. C. Coerwinkel, M. Kristensen, and J. P. Woerdman, "Helical-wavefront laser beams produced with a spiral phase plate," Opt. Commun. **112**(5-6), 321–327 (1994).

[3] W. M. Lee, X. C. Yuan, and W. C. Cheong, "Optical vortex beam shaping by use of highly efficient irregular spiral phase plates for optical micromanipulation," Opt. Lett. **29**, 1796-1798 (2004).

[4] J. Leach, E. Yao, and M. J. Padgett, "Observation of the vortex structure of a non-integer

vortex beam," New J. Phys. **6**(1), 71 (2004).

[5] S. S. R. Oemrawsingh, J. A. W. van Houwelingen, E. R. Eliel, J. P. Woerdman, E. J. K. Verstegen, J. G. Kloosterboer, and G. W. 't Hooft, "Production and characterization of spiral phase plates for optical wavelengths," Appl. Opt. **43**, 688-694 (2004).

[6] M. W. Beijersbergen, L. Allen, H. E. L. O. van der Veen, and J. P. Woerdman, "Astigmatic laser mode converters and transfer of orbital angular momentum," Opt. Commun. **96**, 123–132 (1993).

[7] L. Allen, M. W. Beijersbergen, R. J. C. Spreeuw, and J. P. Woerdman, "Orbital angular momentum of light and the transformation of Laguerre-Gaussian laser modes," Phys. Rev. A. **45**, 8185–8189 (1992).

[8] S. C. Chu, Y. T. Chen, K. F. Tsai, K. Otsuka, "Generation of high-order Hermite-Gaussian modes in end-pumped solid state lasers for square vortex array laser beam generation," Opt. Express **20**, 7128–41 (2012).

[9] S. C. Chu, Y. T. Chen, K. F. Tsai, K. Otsuka, "Generation of high-order Hermite-Gaussian modes in end-pumped solid state lasers for square vortex array laser beam generation," Opt. Express **20**, 7128–41 (2012).

[10] V. V. Kotlyar, A. A. Kovalev, A. P. Porfirev, " Astigmatic laser beams with a large orbital angular momentum," Opt. Express **26**, 141–56 (2018).

[11] N. R. Heckenberg, R. McDuff, C. P. Smith, and A. G. White, "Generation of optical phase singularities by computer-generated holograms," Opt. Lett. **17**, 221-223 (1992)

[12] V. Bazhenov, M. S. Soskin, and M. V. Vasnetsov, "Screw dislocations in light wavefronts," J. Mod. Opt. **39**, 985–990 (1992).

[13] V. Y. Bazhenov, M. V. Vasnetsov, and M. S. Soskin, "Laser-beams with screw dislocations in their wavefronts," JETP. Lett. **52**, 429–431 (1990).

[14] N. R. Heckenberg, R. McDuff, C. P. Smith, H. Rubinsztein-Dunlop, and M. Wegener, "Laser beams with phase singularities," Opt. Quantum. Electron **24**, S951–S962 (1992).

[15] N. Matsumoto, T. Ando, T. Inoue, Y. Ohtake, N. Fukuchi, T. Hara, "Generation of high-quality higher-order Laguerre-Gaussian beams using liquid-crystal-on-silicon spatial light modulators," J. Opt. Soc. A. **25**, 1642–1651 (2008).

[16] A. Jesacher, A. Schwaighofer, S. Fürhapter, C. Maurer, S. Bernet, and M. Ritsch-Marte, "Wavefront correction of spatial light modulators using an optical vortex image," Opt. Express **15**(9), 5801–5808 (2007).

[17] A. Forbes, A. Dudley, and M. McLaren, “Creation and detection of optical modes with spatial light modulators,” Adv. Opt. Photonics **8**(2), 200-227 (2016).

[18] D. Spangenberg, A. Dudley, P. H. Neethling, E. G. Rohwer, and A. Forbes, “White light wavefront control with a spatial light modulator,” Opt. Express **22**, 13870–13879 (2014).

[19] B. Boruah, “Dynamic manipulation of a laser beam using a liquid crystal spatial light modulator,” Am. J. Phy. **77**, 331–336 (2009).

[20] Y. Ohtake, T. Ando, N. Fukuchi, N. Matsumoto, H. Ito, and T. Hara, “Universal generation of higher-order multiringed Laguerre-Gaussian beams by using a spatial light modulator,” Opt. Lett. **32**, 1411-1413 (2007)

[21] Y. F. Chen, Y. P. Lan, and S. C. Wang, “Generation of Laguerre–Gaussian modes in fiber-coupled laser diode end-pumped lasers,” Appl. Phys. B, **72** (2), 167-170 (2001).

[22] J..W. Kim, “High-power laser operation of the first-order Laguerre-Gaussian ($LG_{01}$) mode in a diode-laser-pumped Nd: YAG laser,” J. Korean Phys. Soc. **61**, 739–743 (2012).

[23] Y. Senatsky, J.-F. Bisson, J. Li, A. Shirakawa, M. Thirugnanasambandam, and K. Ueda, “Laguerre-Gaussian modes selection in diode-pumped solid-state lasers,” Opt. Rev. **19**, 201 (2012).

[24] J. W. Kim, and W. A. Clarkson. “Selective generation of Laguerre–Gaussian (LG0n) mode output in a diode-laser pumped Nd: YAG laser,” Opt. Commun. **296**, 109-112 (2013).

[25] D. J. Kim, J. W. Kim, and W. A. Clarkson, “Q-switched Nd:YAG optical vortex lasers,” Opt. Express **21**, 29449-29454 (2013).

[26] D. Lin, J. M. O. Daniel, and W. A. Clarkson, “Controlling the handedness of directly excited Laguerre–Gaussian modes in a solid-state laser,” Opt. Lett. **39**, 3903-3906 (2014).

[27] D. Kim and J. Kim, “Direct generation of an optical vortex beam in a single-frequency Nd:$YVO_4$ laser,” Opt. Lett. **40**, 399–402 (2015).

[28] A. Ito, Y. Kozawa, and S. Sato, “Generation of hollow scalar and vector beams using a spot defect mirror,” J. Opt. Soc. A. **27**, 2072–2077 (2010).

[29] K. Kano, Y. Kozawa, and S. Sato, “Generation of purely single transverse mode vortex beam from a He-Ne laser cavity with a spot-defect mirror,” Int. J. Opt. 2**0**, 359141 (201**2**).

[30] A. J. Lee, T. Omatsu, and H. M. Pask, “Direct generation of a first-Stokes vortex laser beam from a self-Raman laser,” Opt. Express **21**, 12401–12408 (2013).

[31] A. J. Lee, C. Zhang, T. Omatsu, and H. M. Pask, “An intracavity, frequency-doubled self-Raman vortex laser,” Opt. Express **22**, 5400–5409 (2014).

[32] A. J. Lee, H. M. Pask, and T. Omatsu, “A continuous-wave vortex Raman laser with sum frequency generation,” Appl. Phys. B. **122**, 64 (2016).

[33] S. Ngcobo, I. Litvin, L. Burger, and A. Forbes, “A digital laser for on-demand laser modes,” Nat. Commun. **4**, 2289 (2013).

[34] I. A. Litvin, S. Ngcobo, D. Naidoo, K. Ait-Ameur, and A. Forbes, “Doughnut laser beam as an incoherent superposition of two petal beams,” Opt. Lett. **39**, 704-707 (2014).

[35] A. Forbes, N. C. du Preez, V. Belyi, and L. R. Botha, “The digital laser: on-demand laser modes with the click of a button,” Proc. SPIE **8960**, 89601K (2014).

[36] X. Wang, Z. Nie, Y. Liang, J. Wang, T. Li, and B. Jia, “Recent advances on optical vortex generation,” Nanophotonics **7**, 1533–1556 (2018).

[37] J. Arlt and M. J. Padgett, “Generation of a beam with a dark focus surrounded by regions of higher intensity: the optical bottle beam,” Opt. Lett. **25**, 191-193 (2000).

[38] B. P. S. Ahluwalia, X. C. Yuan, and S. H. Tao, “Generation of self-imaged optical bottle beams,” Opt. Commun. **238**, 177-184 (2004).

[39] P. Zhang, Z. Zhang, J. Prakash, S. Huang, D. Hernandez, M. Salazar, D. N. Christodoulides, and Z. Chen, “Trapping and transporting aerosols with a single optical bottle beam generated by moiré techniques, ” Opt. Lett. **36**, 1491-1493 (2011).

[40] D. McGloin, G. C. Spalding, H. Melville, W. Sibbett, and K. Dholakia, “Three-dimensional arrays of optical bottle beams,” Opt. Commun. **225**(4-6), 215-222 (2003).

[41] M. D. Wei, W. L. Shiao, and Y. T. Lin, “Adjustable generation of bottle and hollow beams using an axicon,” Opt. Commun. **248**, 7-14 (2005).

[42] J. H. Lin, M. D. Wei, H. H. Liang, K. H. Lin, and W. F. Hsieh, “Generation of supercontinuum bottle beam using an axicon,” Opt. Express **15(6)**, 2940-2946 (2007).

[43] F. Wu, W. Lu, and B. Liu, “Generation of self-imaged optical bottle beam by using axicons,” In Solid State Lasers and Amplifiers IV, and High-Power Lasers. **7721**, 77211C (2010).

[44] M. D. Wei, “Generation of bottle beam by focusing a super-Gaussian beam using a lens and an axicon,” Opt. Commun. **277**(1), 19-23 (2007).

[45] T. Du, T. Wang, and F. Wu, “Generation of three-dimensional optical bottle beams via focused non-diffracting Bessel beam using an axicon,” Opt. Commun. **317**, 24-28 (2014).

[46] J. Courtial, K. Dholakia, L. Allen, and M. J. Padgett “Second-harmonic generation and the conservation of orbital angular momentum with high-order Laguerre-Gaussian modes,” Phys. Rev. A **56**, 4193-4196 (1997).
[47] P. T. Tai, W. F. Hsieh, and C. H. Chen, “Direct generation of optical bottle beams from a tightly focused end-pumped solid-state laser,” Opt. Express **18(24)**, 5827-5833 (2004).
[48] C. H. Chen, P. T. Tai, and W. F. Hsieh, “Bottle beam from a bare laser for single-beam trapping,” Appl. Opt. **43**, 6001-6006 (2004).

# 4 Nonlinear frequency conversion processes

Solid-state lasers mostly operate at a near-infrared region. To extend further the lasing wavelength of the solid-state lasers, second order nonlinear optical processes, such as second harmonic generation (SHG), sum frequency generation (SFG), and difference frequency generation (DFG), have been conducted. In particular, SHG is commonly used to convert the near-infrared solid-state lasers into visible light sources at high efficiency.

Also, stimulated Raman scattering (SRS), well-known third-order nonlinear optical process, has been proved to be promising to fill in a frequency gap of laser emissions.

## 4.1 Second harmonic generation

Franken *et al.* (1961) have, for the first time, demonstrated SHG [1,2], in which a red ruby laser output (694.3 nm) was focused onto a quartz crystal and its ultraviolet second harmonics (347.15 nm) was then observed. Here, in order to describe such second order nonlinear effects, the polarization $P(t)$ including nonlinear terms can be described by

$$\begin{aligned} P(t) &= \epsilon_0 \left[\chi^{(1)}E(t) + \chi^{(2)}E^2(t) + \chi^{(3)}E^3(t) + \cdots\right] \\ &= P^1(t) + P^2(t) + P^3(t) + \cdots \end{aligned} \tag{4.1.1}$$

where $E(t)$ is the electric field, $\epsilon_0$ is the dielectric constant of vacuum, $\chi^{(1)}$ is the electric susceptibility, and $\chi^{(2)}$ and $\chi^{(3)}$ are the second- and third-order nonlinear optical susceptibilities, respectively. Also, $P^1(t)$ is the linear polarization, $P^2(t)$ and $P^3(t)$ are presented as the second- and third-order nonlinear polarizations, respectively. In general, the second-order nonlinear polarization occurs only in the noncentrosymmetric materials with the inversion symmetry breaking. In contrast, third-order nonlinear polarization always appears in both centrosymmetric and noncentrosymmetric crystals.

In this section, we present a brief description of the SHG process, as illustrated schematically in Fig. 4.1.

Here, the electric field of the incident laser beam on a nonlinear medium can be expressed as

$$E(\mathrm{t}) = E_{\omega_1}\, e^{-i\omega_1 t} + c.c \tag{4.1.2}$$

The nonlinear polarization is then given according to Eq. (4.1) as

$$P^2(t) = 2\epsilon_0\chi^{(2)}E_{\omega_1}E_{\omega_1}{}^* + (\epsilon_0\chi^{(2)}E_{\omega_1}^2 e^{-i2\omega_1 t} + c.c) \quad (4.1.3)$$

The second term on the right of the Eq. (4.3) contributes to the second-harmonic frequency $2\omega_1 = \omega_2$, and it leads to the SHG process.

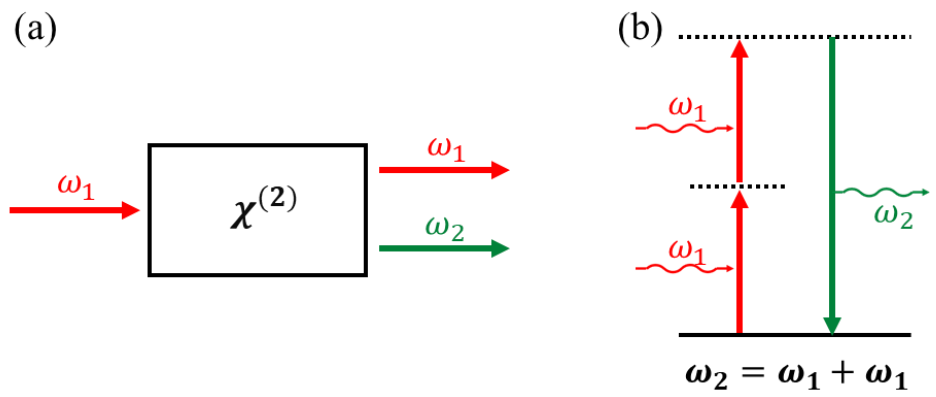


Fig. 4.1 (a) Geometry of second-harmonic generation. (b) Energy-level Schematic of second-harmonic generation.

We consider the nonlinear interaction between two waves written as

$$E^{\omega_1}(z,t) = E_1 e^{i(\omega_1 t - k_1 z)} + \text{c. c.} \quad (4.1.4)$$

$$E^{\omega_2}(z,t) = E_2 e^{i(\omega_2 t - k_2 z)} + \text{c. c.} \ . \quad (4.1.5)$$

Thus, the total electric field within the nonlinear crystal can be given by

$$E = E^{\omega_1}(z,t) + E^{\omega_2}(z,t) \quad (4.1.6)$$

The term of nonlinear polarization can, here, be represented as

$$P_{NL} = P_{NL}^{\omega_1}(z,t) + P_{NL}^{\omega_2}(z,t) \quad (4.1.7)$$

where

$$P_{NL}^{\omega_1}(z,t) = 4\epsilon_0 d E^{\omega_2}(z,t) E^{\omega_1 *}(z,t) = 4\epsilon_0 d E_2 E_1^* e^{i[(\omega_2-\omega_1)t-(k_2-k_1)z]} \quad (4.1.8)$$

$$P_{NL}^{2\omega_1}(z,t) = 2\epsilon_0 d E^{\omega_1}(z,t) E^{\omega_1}(z,t) = 2\epsilon_0 d E_1 E_1 e^{i(2\omega_1 t-2k_1 z)} \quad . \quad (4.1.9)$$

The nonlinear wave equation can be then written as

$$\nabla^2 \boldsymbol{E} = \mu_0 \frac{\partial^2}{\partial t^2}(\epsilon_0 \boldsymbol{E} + \boldsymbol{P}) = \mu_0 \epsilon \frac{\partial^2 E}{\partial t^2} + \mu_0 \frac{\partial^2}{\partial t^2} P_{NL} \quad (4.1.10)$$

, where $P_{NL}$ is the nonlinear polarization.

By employing the slowly varying approximation, the coupled wave equation for SHG can be given as

$$\frac{\mathrm{d}}{\mathrm{dz}} E_1 = -i\omega_1 \sqrt{\frac{\mu_0}{\varepsilon_1}} d E_2 E_1^* e^{-i(k_2-2k_1)z} \quad (4.1.11)$$

$$\frac{\mathrm{d}}{\mathrm{dz}} E_2 = -i\omega_2 \sqrt{\frac{\mu_0}{\varepsilon_2}} \frac{1}{2} d E_1 E_1 e^{+i(k_2-2k_1)z} \quad (4.1.12)$$

, where we introduce the quantity $\Delta k = k_2 - 2k_1$, that is a phase mismatching. The special case $\Delta k = 0$ is also dubbed the phase matching condition.

Under the undepleted-pumped condition, the second harmonic electric field through the material (with a length of $L$ ) is easily obtained as

$$E_2(L) = -i\omega_1 \sqrt{\frac{\mu_0}{\varepsilon}} d E_1^2 \frac{e^{+i(\Delta k)L}-1}{i(\Delta k)L} L \quad (4.1.13)$$

The resulting second harmonic intensity is expressed by

$$I^{(2\omega_1)} = 1/2 c_0 n \varepsilon_0 |E_2(L)|^2 \quad (4.1.14)$$

The corresponding SHG conversion efficiency $\eta_{SHG}$ can be addressed as

$$\eta_{SHG} = \frac{I^{(2\omega_1)}}{I^{(\omega_1)}} = \frac{2{\omega_1}^2 d^2 L^2}{n^3} \left(\frac{\mu_0}{\varepsilon_0}\right)^{3/2} \frac{sin^2[(\Delta k)L/2]}{[(\Delta k)L/2]^2} I^{(\omega_1)} \quad (4.1.15)$$

Interestingly, the second harmonic field intensity is proportional to the square of the fundamental field intensity when $\Delta k = 0$. Note that the conversion efficiency is very

sensitive to the phase mismatching $\Delta k$.

There are several nonlinear crystals used for SHG, such as potassium titanyl phosphate (KTP), lithium triborate (LBO), and beta-barium borate ($\beta$-BBO). Table 4.1 shows physical properties of the nonlinear crystals.

Table 4.1 Properties of three nonlinear crystals in the SHG (1064 nm to 532 nm) process [3].

| Properties | KTP | LBO | $\beta$-BBO |
|---|---|---|---|
| Effective nonlinear coefficient $d$ (pm/V) | 4.03 (Type II) | 0.82 (Type I) | 2.14 (Type I)<br>1.47 (Type II) |
| Walk-off angle (mrad) | 4.87 (Type II) | 6.7 (Type I)<br>6.4 (Type II) | 55.6 (Type I)<br>69.4 (Type II) |
| Phase-matching wavelength (nm) | 994-2000 (Type II) | 551-2600 (Type I)<br>790-2150 (Type II) | 410-3500 (Type I)<br>525-3500 (Type II) |

A KTP is an excellent nonlinear crystal for intracavity SHG with large nonlinearity, wide acceptance frequency width, and small walk-off effect for 1064 nm (see Tab. 4.1). In this thesis, we decided that the KTP crystal was used as a nonlinear crystal for intracavity SHG in chapter 7.

## 4.2 Stimulated Raman Scattering

In 1962, Woodbury and Ng discovered the phenomenon of stimulated Raman scattering (SRS) [4], and then Eckhardt *et al.* gave a more detailed description [5]. In the Raman scattering process illustrated in Fig. 4.3, a fundamental photon with a frequency $\omega_p$ is annihilated and a Stokes photon with a frequency $\omega_s = \omega_p - \omega_v$ is emitted, where $\hbar\omega_v$ corresponds to vibrational energy. The Stokes photon is coherently amplified via nonlinear wave coupling process, thereby yielding the coherent Stokes electric field, that is stimulated Raman scattering (SRS).

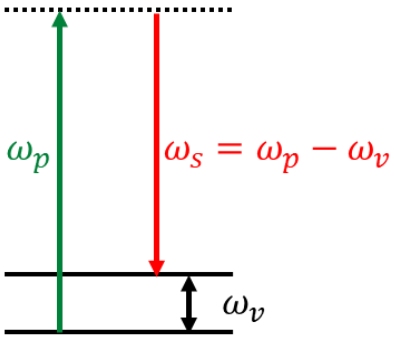


Fig. 4.3 Stimulated Raman Scattering.

The SRS is described classically by nonlinear polarization [6] based on a scalar approximation. The total electric field can be represented as the sum of the fundamental and Stokes fields,

$$E(z,t) = E_p e^{i(k_p z - \omega_p t)} + E_s e^{i(k_s z - \omega_s t)} + \text{c. c.} \quad . \tag{4.2.15}$$

The corresponding Stokes polarization is written as

$$P_{NL}^{\omega_s}(z,t) = 6\epsilon_0 \chi_R^{(\omega_s)} |E_p|^2 E_s e^{i(k_s z - \omega_s t)} + \text{c. c.} \tag{4.2.16}$$

, where $\chi_R^{(\omega_s)}$ is the Raman activity described as [6]

$$\chi_R^{(\omega_s)} = -i \frac{\epsilon_0 (N/6m)(\partial\alpha/\partial q)_0^2}{2\omega_v \gamma} \quad . \tag{4.2.17}$$

By utlizing Eqs. (4.15) and (4.16) under the slowly varying approximation, the spatial evolution of the Stokes field $E_s$ is given as follows:

$$\frac{dE_s}{dz} = 3i \frac{\omega_s}{n_s c} \chi_R^{(\omega_s)} |E_p|^2 E_s \tag{4.2.18}$$

It is noteworthy that the phase-matching condition in SRS is automatically satisfied.

A variety of SRS crystals have been reported [7]. These Raman crystals have considerable potential to develop a new generation of solid-state lasers, including diode-pumped devices.

In fact, Raman solid-state lasers have currently made significant progress owing to the development of crystal growth technologies. Tables 4.2 and 4.3 summarize the commonly used Raman crystals with high Raman activities and excellent thermal properties.

Table 4.2 SRS spectral properties of conventional Raman crystals [8-12]

| Crystals | Raman Shift ($cm^{-1}$) | Raman Linewidth $\Delta v_R$($cm^{-1}$) | Cross-section (arb. Units) | Raman Gain $g_R$(cm/GW) |
|---|---|---|---|---|
| Diamond | 1332 | 2.7 | 100 | 20 |
| $Ba(NO_3)_2$ | 1047 | 0.4 | 21 | 11 |
| $KGd(WO_4)_2$ | 768 | 6.7 | 59 | 4.4 |
| | 901 | 5.7 | 54 | 3.3 |
| $BaWO_4$ | 924 | 1.6 | 52 | 8.5 |
| $YVO_4$ | 890 | 2.6 | 92 | > 4.5 |
| $GdVO_4$ | 882 | 3 | 92 | > 4.5 |

Table 4.3 Thermal properties of conventional Raman crystals [8-12]

| Crystal | Thermal conductivity κ (W/mK) | Thermal expansion ($10^{-6}$ $K^{-1}$) | dn/dT ($10^{-6}$ ) | Damage threshold ($GW/cm^2$) |
|---|---|---|---|---|
| Diamond | >1800 | 1.1 | ~ 20 | ~ 1.5 |
| $Ba(NO_3)_2$ | 1.17 | 18 | -20 | ~ 0.4 |
| $KGd(WO_4)_2$ | 2.6 (a) | 2.4 (a) | -1.5 (a) | ~ 10 |
| | 3.8 (b) | 11 (b) | -1.0 (b) | |
| | 3.4 (c) | 17 (c) | -1.6 (c) | |
| $BaWO_4$ | 2.3 | 4-6 | -9 | ~ 5 |
| $YVO_4$ | 5.1 | 4.43 (a) | 2.7 | ~ 1 |
| | | 11.37 (c) | | |
| $GdVO_4$ | 11.7 | 1.5 (a) | 4.7 | ~ 1 |
| | | 7.3 (c) | | |

In particular, a diamond has the highest Raman gain coefficient (20 cm/GW) and excellent thermal properties. The first observation of SRS in diamonds was discovered in 1963 [8-9].

The chemical-vapor-deposition (CVD) technique currently enables us to manufacture high-quality diamonds, thereby enabling the realization of a 'diamond laser'.

Several tungstate crystals, including double tangstates, such as $KGd(WO_4)_2$ and $KY(WO_4)_2$, and single tangstates, such as $BaWO_4$, $CaWO_4$, $SrWO_4$, and $PbWO_4$, have been also found to have the excellent physical properties for Raman lasers. Interestingly, several tungstate crystals with the doping of trivalent rare-earth ions further act as a laser gain medium, so as to develop compact self-Raman laser sources.

The vanadate crystals, such as $YVO_4$ and $GdVO_4$, were first introduced as Raman crystals in 2001[12]. The vanadates have been widely used as a host laser crystal to develop diode-pumped solid-state lasers with high efficiencies. In fact, Nd:$YVO_4$ and Nd:$GdVO_4$ crystals with excellent mechanical, physical, and thermal properties have been commercialized. Also, both Nd:$YVO_4$ and Nd:$GdVO_4$ crystals are naturally birefringent, and their laser outputs are linearly polarized, thereby allowing the highly efficient intracavity SHG and SFG without any thermally-induced birefringence effects.

In this work, we used a-cut Nd:$GdVO_4$ crystal as a self-Raman laser crystal to develop ultra-compact LG mode laser source mentioned in Chapter 5. Table 4.4 summarizes physical properties of Nd:$GdVO_4$.

Table 4.4 The properties of Nd:$GdVO_4$ crystals

| Parameter | Value |
|---|---|
| Refractive index | $n_o$=1.985<br>$n_e$=2.198 |
| Effective Laser Cross Section<br>(emission cross section at 1064 nm) | $7.6\times10^{-19}$ (E//c) |
| Fluorescence lifetime (μs) | 95 |
| Polarization | Parallel to c-axis |

# 4.3 References

[1] P. A. Franken, A. E. Hill, C. W. Peters, G. Weinreich, "Generation of Optical Harmonics," Phy. Rev. Lett. **7**(4), 118-119 (1961).

[2] R. L. Byer, “Nonlinear Optics and Solid-State Lasers: 2000,” IEEE J. Quantum Electronics **6**(6), 911-930 (2000).

[3] https://www.alphalas.com

[4] E. J. Woodbury and W. K. Ng, “Ruby laser operation in the near IR,” Proc. IRE **50**, 2367 (1962).

[5] G. Eckhardt, R. W. Hellwarth, F. J. McClung, S. E. Schwarz, D. Weiner, and E. J. Woodbury, “Stimulated Raman scattering from organic liquids,” Phys. Rev. Lett. **9**, 455–457 (1962).

[6] N. Bloembergen, *Nonlinear Optics.* New York: Benjamin, 1965.

[7] H. M. Pask, “The design and operation of solid-state Raman lasers,” Progress in Quantum Electronics **27**(1), 3-56 (2003).

[8] G. Eckhardt, D. Bortfeld, and M. Geller, “Stimulated emission of Stokes and anti-Stokes Raman lines from diamond, calcite and α-sulfur single crystals,” Appl. Phys. Lett. **3**(8), 137 (1963).

[9] A. K. McQuillan, W. R. L. Clements, and B. P. Stoicheff, “Stimulated Raman emission in Diamond: spectrum, gain, and angular distribution of intensity,” Phys. Rev. A **1**(3), 628 (1970).

[10] P. G. Zverev, J. T. Murray, R. C. Powell, R. J. Reeves, and T. T. Basiev, “Stimulated Raman scattering of picosecond pulses in barium nitrate crystals,” Opt. Commun. **97**, 59-64 (1993).

[11] P. Cerny, P. G. Zverev, H. Jelinkova, T. T. Basiev, “Efficient Raman shifting of picosecond pulses using $BaWO_4$ crystal,” Opt. Commun. **177**, 397–404 (2000).

[12] A. A. Kaminskii, K. Ueda, H. J. Eichler, Y. Kuwano, H. Kouta, S. N. Bagaev, T. H. Chyba, J. C. Barnes, G. M. A. Gad, T. Murai, L. Jianren, “Tetragonal vanadates $YVO_4$ and $GdVO_4$–new efficient $\chi^{(3)}$-materials for Raman lasers,” Opt. Commun. **194**, 201–206 (2001).

# 5. Self-Raman Nd:$GdVO_4$ vortex laser

## 5.1 Background

Stimulated Raman scattering (SRS), a well-known third-order nonlinear frequency conversion, is capable of filling in a wavelength gap of laser sources [1-5], in particular, at the near-infrared and visible regions, with the aid of second order nonlinear frequency conversions, such as SHG or sum-frequency generation (SFG). A variety of laser host media, such as $YVO_4$ [6-9], $GdVO_4$ [9-13], $SrWO_4$ [14,15], $BaWO_4$[16-18], and $PbWO_4$ [19-21] exhibit excellent SRS properties. Thus, they can act as laser and Raman gain media simultaneously, thereby allowing us to realize ultracompact and highly efficient solid-state lasers, so-called self-Raman lasers, with the wavelength versatility.

In recent years, there have been considerable efforts to develop Nd: $GdVO_4$ self-Raman vortex laser sources, in which the Stokes (1.173 μm) output operates at a first order LG mode owing to the 882 $cm^{-1}$ shift, by employing an output coupler with a laser micro-machined damage spot [10-12], however, there are still no reports of vortex laser sources operating at 1.108 μm, corresponding to 382 $cm^{-1}$ shift with a ~6.4 times smaller Raman gain than that of 882 $cm^{-1}$ shift [11] (see Fig 5.1 and Table 5.1).

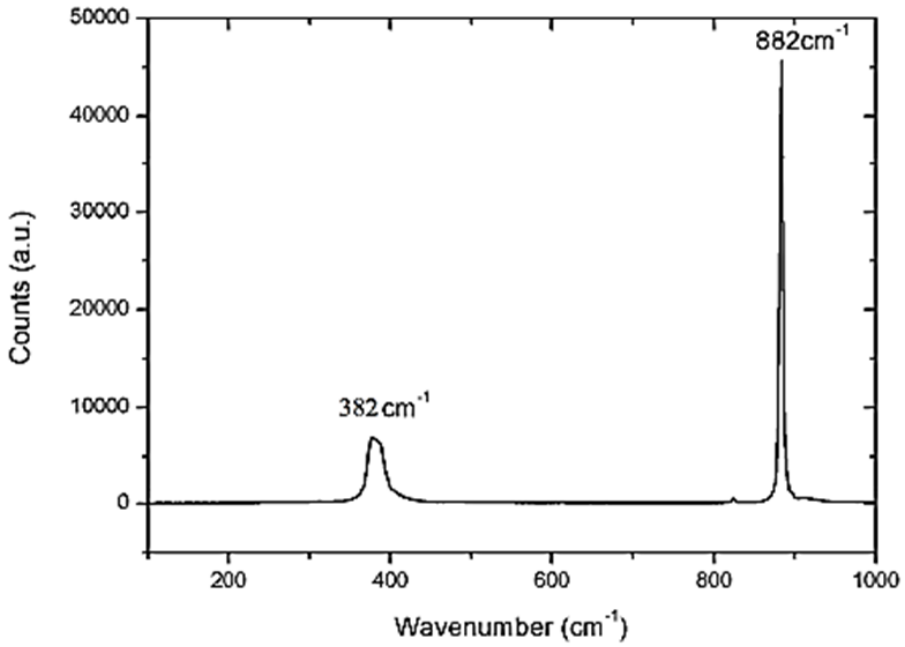


Fig. 5.1 Polarized Raman spectrum of *a*-cut Nd:$GdVO_4$ crystal.

Tab. 5.1 Specifications for Raman transitions of *a*-cut Nd:$GdVO_4$ crystal.

| Nd:$GdVO_4$ Raman transition | Raman shift ($cm^{-1}$) | Raman gain $g_R$ (cm/GW) | Stokes wavelength (μm) |
|---|---|---|---|
| $\nu_1$ | 882 | 4.5 | 1.173 |
| $\nu_2$ | 382 | 0.7 | 1.108 |

In this section, I propose a novel approach to generate LG modes from a self-Raman Nd: $GdVO_4$ laser by employing a shaped pumping geometry formed of an axicon lens and an objective lens. The system allows us to generate selectively a first-order LG mode at 1.108 μm or 1.173 μm or both 1.108 μm and 1.173 μm only by carefully aligning the output coupler. Maximum output powers of 49.8 mW and 133.4 mW for the wavelengths of 1.108 μm and 1.173 μm were then measured at the absorbed pump power of 5.69 W.

## 5.2 Experiments

Figure 5.2 (a) shows the experimental setup for the self-Raman laser. A 10-mm-long $Nd^{3+}$: $GdVO_4$ *a*-cut crystal with 0.3 at.% Nd doping was conducted as a laser gain medium. The crystal was wrapped with an indium foil, and it was mounted inside a copper block holder, so as to maintain its temperature (~20°C) by a circulating water-cooled chiller.

A fiber-coupled laser diode (nLight element e06; core diameter: 200 μm, numerical aperture: 0.22) with a wavelength of 879 nm was used as a pump source, and its output was collimated by a lens (CL, $f$ = 25 mm). The collimated pump diode beam was shaped to be an annular beam by an axicon lens with an Axicon angle of 5°, and it was focused by a relay optics, formed of a lens (IL, $f$ = 25mm) and an infinity-corrected objective lens (ICO, $f$ = 200 mm), on the crystal. It is also worth noting that the polarization of the pump beam was parallel to the *c*-axis of the crystal, thereby yielding maximum absorption (absorption efficiency ~76 %) of the laser gain medium.

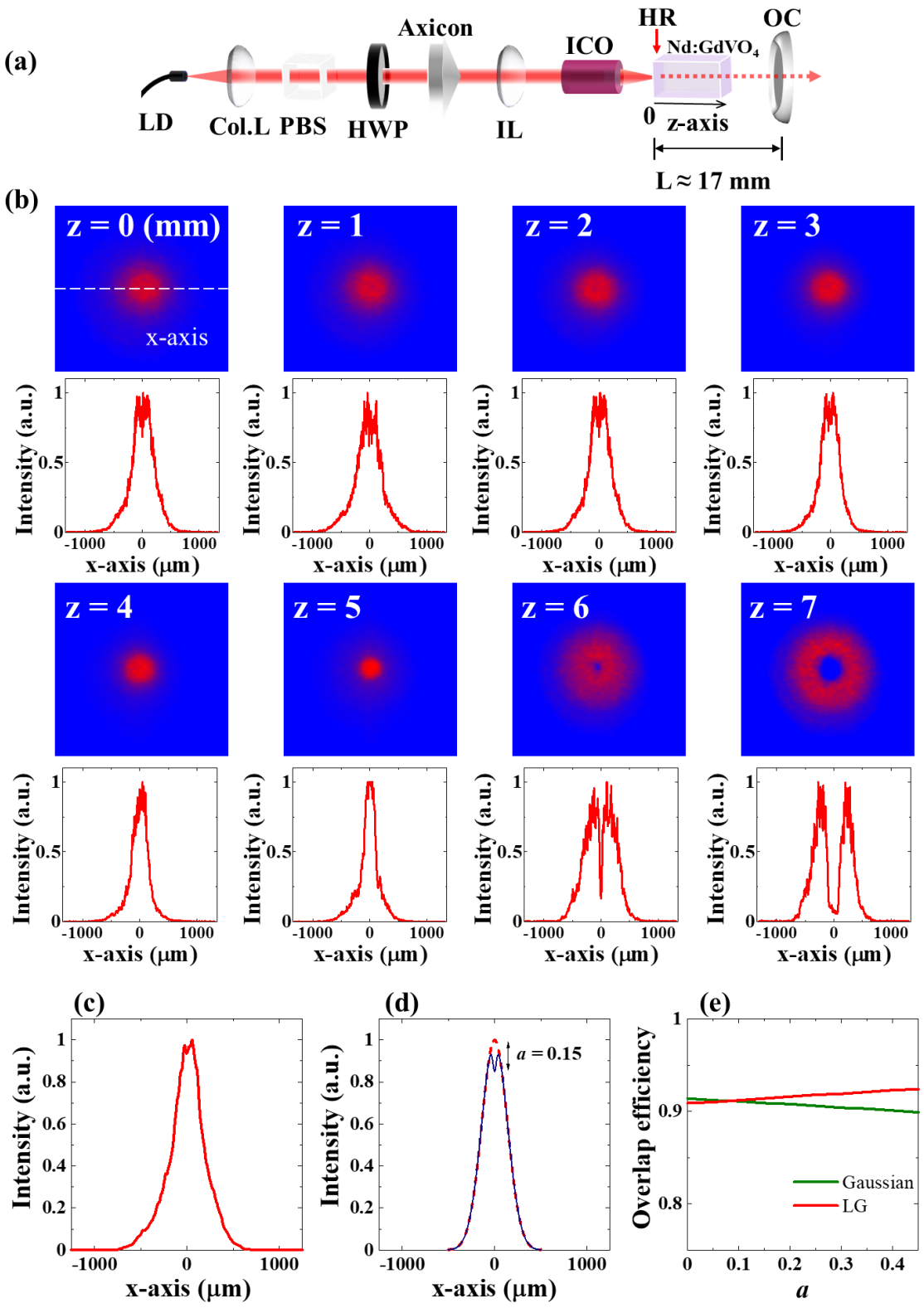


Fig. 5.2 (a) Direct generation of LG modes from a continuous-wave diode-pumped self-Raman Nd: $GdVO_4$ laser. LD: 879 nm fiber-coupled laser diode (nLight element e06); Col.

L: collimation lens ( $f$ = 25 mm); PBS: polarized beam splitter; HWP: half-wave plate; IL: lens ( $f$ = 25 mm); ICO: NIR infinity-corrected objectives ( $f$ = 200 mm, 10X / 0.26); HR: high-reflection coating for 1.033-1.263 μm; OC: output coupler. (b) Beam propagation of the pump beam along the optical axis of the laser cavity. (c) Effective pumped region in the crystal. (d) Modelled pumped region for simulating spatial overlap efficiency. The red broken and black solid lines correspond to those at $a$ = 0 and 0.15, respectively. (e) Simulated spatial overlapping efficiency as a function of dip depth $a$.

This pump geometry allows us to shape the pump beam with a central intensity dip, thus, we will expect the improvement of the spatial overlap between the pump beam and LG mode. In fact, the effective pumped region $g(r)$ in the pump facet can be estimated as the following formula,

$$g(r) \propto \sum_i P(r, \Delta z \cdot i)\,(1 - e^{-\alpha \Delta z})^i (\alpha \Delta z) \tag{5.2.1}$$

, where $r$ is the radial coordinate in the cylindrical coordinate, $\alpha$ is the absorption coefficient of the pump beam in the crystal, $\Delta z$ is the infinitesimal displacement along the propagation direction ($z$ axis), $i$ is the integer, and $P(r, \Delta z \cdot i)$ is the spatial form of the pumped beam at the position $z \cdot i$ along the propagation direction. The $g(r)$ was estimated by employing eq. (5.2.1) and the experimental spatial forms of the pump beam (Fig. 5.2(b)), The resulting $g(r)$ showed a central shallow dip, which forces the laser to selectively operate at an annular mode with a central dark core instead of Gaussian mode (Fig. 5.2(c)).

For simplicity, it is worth noting that the pumped region $g(r)$ is assumed to be approximately written by the below mentioned formula,

$$g(r) \propto \exp\left(\frac{-2r^2}{\omega_0^2}\right)\left(a \tanh\left(\frac{r^2}{h^2}\right) + (1 - a)\right)^2 \tag{5.2.2}$$

, where $\omega_0$ (~170 μm) and $h$ (= 0.4 $\omega_0$) are the radii of the pump beam and the point defect in the pump beam, and $a$ (0~1) is the depth of the gain dip, respectively. The spatial overlap

η is then given as follows:

$$\eta = \int g(r) \cdot I(r) 2\pi r dr \tag{5.2.3}$$

$$I(r) = r^{2|\ell|} \exp\left(-2\frac{r^2}{\omega_\ell^2}\right) \tag{5.2.4}$$

, where $I(r)$ is the spatial form of the laser mode, ℓ is the topological charge of LG mode, and $\omega_\ell$ (~180 μm, this value was estimated by the LASCAD software) is the intracavity LG mode radius, respectively. In fact, the LG mode exhibits higher spatial overlap within the pump region of $a > 0.1$ compared with that of the fundamental Gaussian mode (see Fig 5.2 (e)).

A self-Raman laser resonator was formed of the input crystal facet with ultrahigh reflection (R > 99.99 %) for 1033-1263 nm and high transmission (T > 99.933%) for 879 nm and a 250 mm concave output coupler (OC) with ultra-high reflection (R > 99.99 %) for 1.063 μm, and high reflectivity (R = 99.99 % and 99.00 %) for 1.108 μm and 1.173 μm. With this extremely high Q cavity, the fundamental (1.063 μm) and Stokes outputs (1.108 μm or 1.173 μm) are allowed to lase simultaneously. It is noteworthy that the OC was translated precisely along the *x*, *y* and *z* axes, thereby selecting the desired laser operation simply by aligning carefully the OC. The cavity length was then fixed to be ~ 17 mm. The fundamental and Stokes outputs were spatially separated by a transmission grating (GR25-0608), so as to observe them simultaneously by a laser beam profiler (Spiricon SP620U).

## 5.3 Results and discussions

The 1.108 μm Stokes output started to lase at the absorbed pump power of 3.52 W, and its output power reached up to 49.8 mW at a maximum pump level (absorbed power of 5.69 W). The fundamental output then exhibited a mixed-mode profile with a central point defect, manifesting several high order transverse modes, owing to extremely high Q factor of the cavity (see Fig.5.2(b)). In contrast, the Stokes output possessed a perfect ring-shaped spatial form with a central dark core in both the near and far-fields, that is a beam clean-up effect, in which the self-Raman gain itself plays a role as an effective soft aperture [22]. There is a

good consistence between the experiments and the simulated spatial overlap.

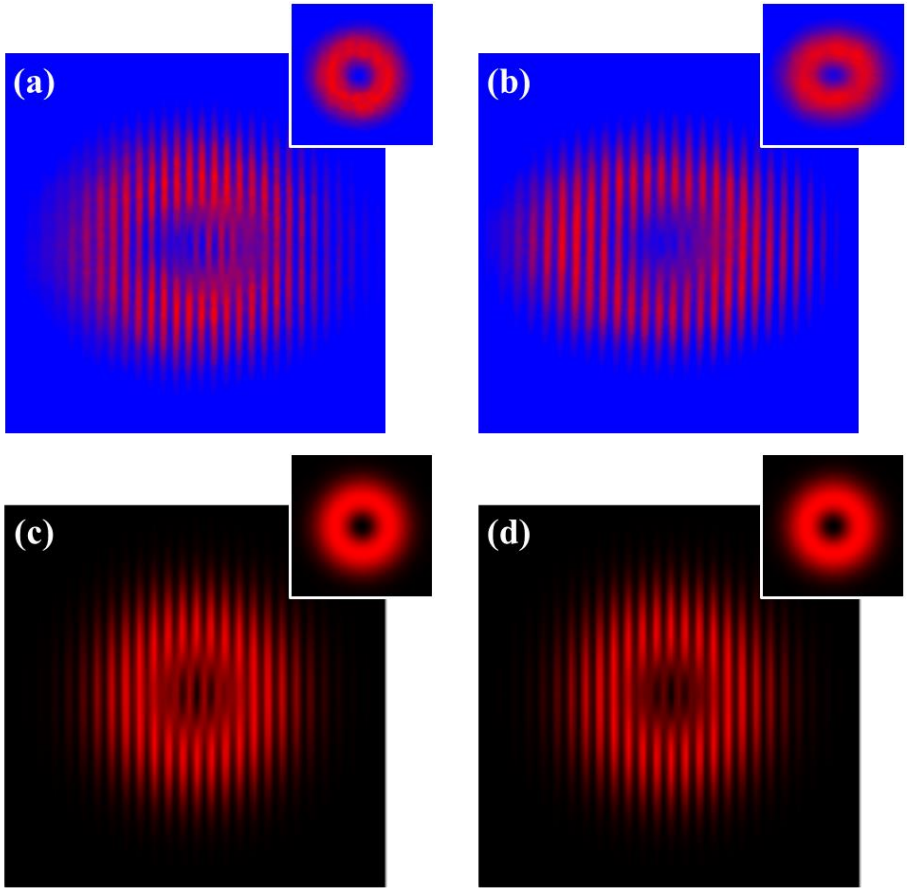


Fig. 5.3 Experimental fringes of (a) 1.108 μm and (b) 1.173 μm Stokes outputs. Insets show the spatial intensity profile of the Stokes output. (c,d) Simulated fringes of incoherent superposition of two LG modes with positive and negative topological charges.

The Stokes output was also analyzed by employing a laterally sheared interferometer based on a transmission grating (10 lines/mm) [23], and it was then found that the Stokes output carries effective zero OAM. The Stoke output was, interestingly, formed of two incoherent LG modes with positive and negative OAMs, originating from the cylindrical symmetry of the laser resonator. In fact, the fringes of the Stokes output will be then given as follows:

$$I(x,y) \propto \left|\left((x+\Delta x)+iy\right)\cdot \exp\left(-\frac{(x+\Delta x)^2+y^2}{\omega_l^2}\right)+e^{ik_x\cdot x}\right|^2+\left|\left((x-\Delta x)-iy\right)\cdot \exp\left(-\frac{(x-\Delta x)^2+y^2}{\omega_l^2}\right)+e^{ik_x\cdot x}\right|^2 \quad (5.2.5)$$

, where $\Delta x$ is the lateral shearing distance of the wavefront, $k_x$ is the carrier frequency of the fringes. As shown in Fig. 5.3, the theoretical formula retrieves well the experimental fringes. The handedness of the LG mode (sign of the vortex beam topological charge) will be selectively controlled by breaking azimuthal symmetry of the laser cavity, for instance, the use of an intracavity etalon or nanoscale aluminum stripes [24-29]. Such selective handedness control of LG mode in this system should be performed as a future work.

The Nd:$GdVO_4$ self-Raman lasers have operated mostly at 1.173 μm, originated from high gain 882 $cm^{-1}$ Raman transition [10-12]. In fact, SRS gain competition between the stronger 882 $cm^{-1}$and a weaker 382 $cm^{-1}$ transitions was observed, however, it is worth noting that the system can operate stably at 1.108 μm after carefully aligning the OC.

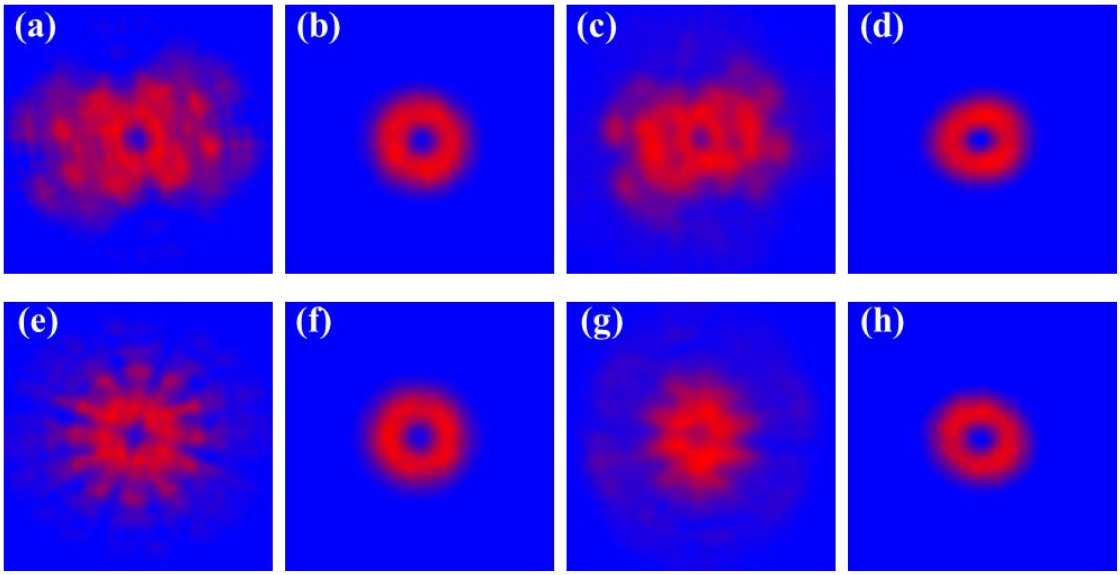


Fig. 5.4 Experimental near-fields of (a) the fundamental (1.063 μm), and (b) 1.108 μm Stokes output. Corresponding far-fields of (c) the fundamental and (d) the Stokes outputs. Experimental near-fields of (e) the fundamental (1.063 μm), and (f) 1.173 μm Stokes outputs. Corresponding far-fields of (g) the fundamental and (h) 1.173 μm Stokes outputs.

Figures 5.4 and 5.5 summarize the experimental spatial forms and the power scaling issues of the fundamental (1.063 μm), and 1.108 μm and 1.173 μm Stokes outputs. The 1.173 μm Stokes output exhibited a relatively high lasing threshold (5.37 W) arising from high transmission loss (~1%), however, its maximum power reached up to 133.4 mW. This value was 2.7 times higher than that of 1.108 μm output. Figure 5.6 also shows the experimental

laser spectra of the fundamental and Stokes outputs by employing a high-resolution optical spectrometer (Ocean-optics HR4000).

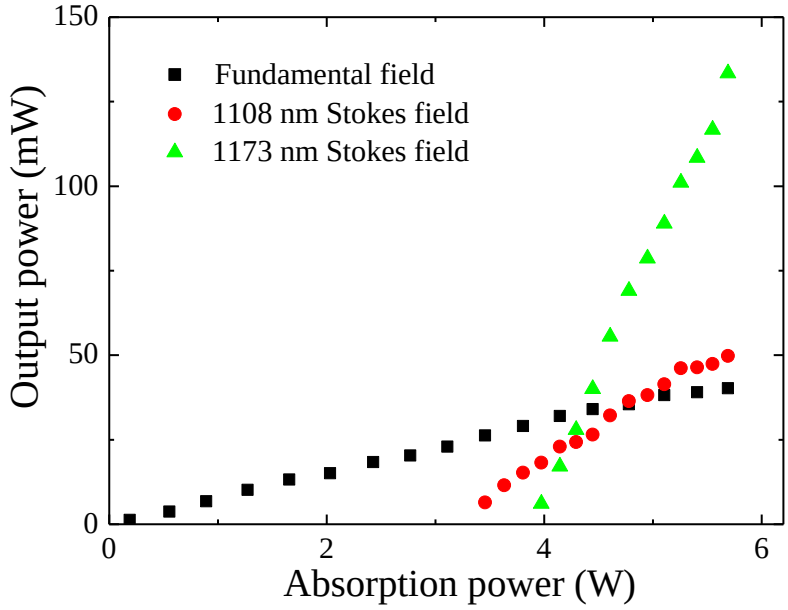


Fig. 5.5 Power scaling of fundamental and Stokes outputs.

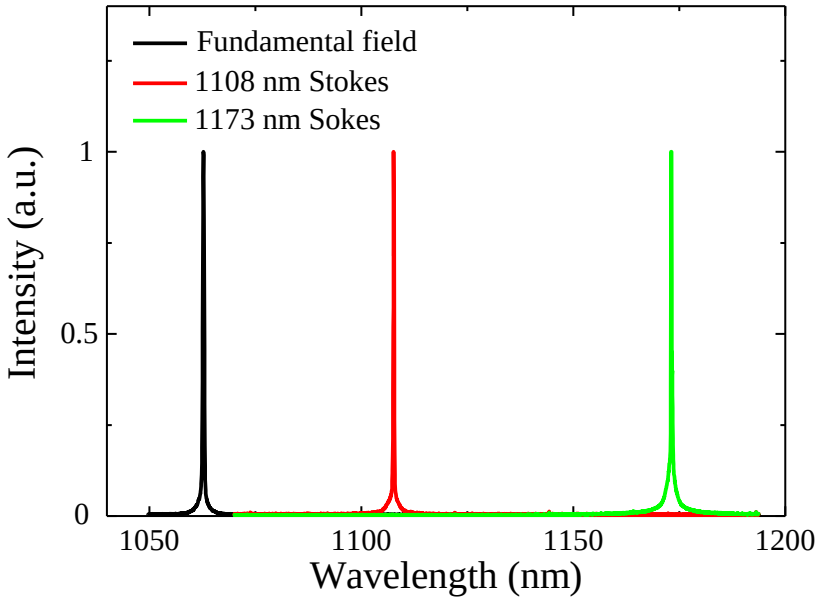


Fig. 5.6 Line spectra of the output modes. Each line is normalized concerning its maximum.

Interestingly, we also achieved a LG mode operation at both 1.108 μm and 1.173 μm (both

LG mode operation) by carefully aligning the OC (see Fig. 5.7). Such both LG mode operation was observed only within the absorbed pump power range of 3.46 – 3.97 W.

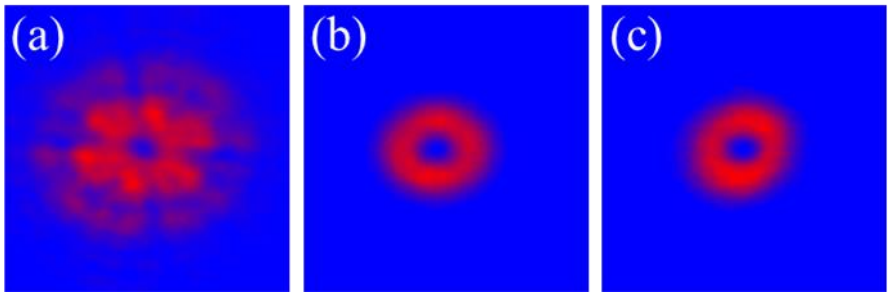


Fig. 5.7 Experimental near-fields of (a) fundamental, and both (b) 1.108 μm and (c) 1.173 μm Stokes outputs.

## 5.4 Conclusion

LG modes at 1.108 μm and 1.173 μm have been directly generated from a continuous-wave self-Raman Nd:$GdVO_4$ laser by utilizing a shaped pumping geometry consisting of an Axicon and a focusing lens. Maximum LG mode powers of 49.8 mW and 133.4 mW were obtained at 1.108 μm and 1.173 μm, respectively. This approach will offer us many benefits, for instance, the stable operation and easy power scaling of the system. Further frequency extension of the system will be possible by employing a SHG or SFG, thereby allowing us to pave the way towards ultracompact ultraviolet/visible LG laser sources.

## 5.5 References

[1] P. Cerny, H. Jelinkova, P. G. Zverev, and T. T. Basiev, “Solid state lasers with Raman frequency conversion,” Prog. Quantum Electron. **28**(2), 113–143 (2004).

[2] J. A. Piper and H. M. Pask, “Crystalline Raman lasers,” IEEE J. Sel. Top. Quantum Electron. **13**(3), 692–704 (2007).

[3] T. T. Basiev and R. C. Powell, “Special issue on solid state Raman lasers - Introduction,” Opt. Mater. **11**, 301-306 (1999).

[4] H. M. Pask, “The design and operation of solid-state Raman lasers,” Prog. Quant. Electron. **27**, 3–56 (2003).

[5] Q. Sheng, H. Ma, R. Li, M. Wang, W. Shi, and J. Yao, “Recent progress on narrow-

linewidth crystalline bulk Raman lasers," Results Phys., 103073 (2020).

[6] H. Zhu, Y. Duan, G. Zhang, C. Huang, Y. Wei, W. Chen, Y. Huang, and N. Ye, "Yellow-light generation of 5.7 W by intracavity doubling self-Raman laser of $YVO_4$/Nd:$YVO_4$ composite," Opt. Lett. **34**(18), 2763–2765 (2009).

[7] Y. F. Chen, "High-power diode-pumped actively Q-switched Nd:$YVO_4$ self-Raman laser: influence of dopant concentration," Opt. Lett. **29**(16), 1915–1917 (2004).

[8] A. Minassian, B. Thompson, and M. Damzen, "Ultrahigh-efficiency $TEM_{00}$ diode-side-pumped Nd:$YVO_4$ laser," Appl. Phys. B **76,** 341–343 (2003).

[9] A. A. Kaminskii, K. Ueda, H. J. Eichler, Y. Kuwano, H. Kouta, S. N. Bagaev, T. H. Chyba, J. C. Barnes, G. M. A. Gad, T. Murai, and J. Lu, "Tetragonal vanadates $YVO_4$ and $GdVO_4$ – new efficient $\chi(3)$ - materials for Raman lasers," Opt. Commun. **194**(1-3), 201–206 (2001).

[10] A. J. Lee, H. M. Pask, D. J. Spence, and J. A. Piper, "Efficient 5.3 W cw laser at 559 nm by intracavity frequency summation of fundamental and first-Stokes wavelengths in a self-Raman Nd:$GdVO_4$ laser," Opt. Lett. **35**(5), 682–684 (2010).

[11] J. Lin and H. M. Pask, "Cascaded self-Raman lasers based on 382 $cm^{-1}$ shift in Nd: $GdVO_4$.," Opt. Express **20**(14), 15180–15185 (2012).

[12] T. Omatsu, M. Okida, A. Lee, and H. M. Pask, "Thermal lensing in a diode-end-pumped continuous-wave self-Raman Nd-doped $GdVO_4$ laser," Appl. Phys. B **108**(1), 73–79 (2012).

[13] A. Minassian, B. A. Thompson, G. Smith and M. J. Damzen, "High-power scaling (>100 W) of a diode-pumped TEM/sub 00/ Nd:GdVO/sub 4/laser system," IEEE J. Sel. Top. Quant. Electronics **11**, 621-625 (2005).

[14] R. Lan, S. Ding, M. Wang, and J. Zhang, "A compact passively Q-switched $SrWO_4$ Raman laser with modelocked modulation," Laser Phys. Lett. **10**(2), 025801 (2013).

[15] F. Yang, Z. You, Z. Zhu, Y. Wang, J. Li, and C. Tu, "End-pumped continuous-wave intracavity yellow Raman laser at 590 nm with $SrWO_4$ Raman crystal," Laser Phys. Lett. **7**, 14 (2009).

[16] P. Černy, P. G. Zverev, H. Jelınková, and T. T. Basiev, "Efficient Raman shifting of picosecond pulses using $BaWO_4$ crystal," Opt. Commun. **177**, 397-404 (2000).

[17] L. Fan, Y. X. Fan, Y. Q. Li, H. Zhang, Q. Wang, J. Wang, and H. T. Wang, "High-efficiency continuous-wave Raman conversion with a $BaWO_4$ Raman crystal," Opt. Lett. **34**, 1687-1689 (2009).

[18] Y. F. Chen, K. W. Su, H. J. Zhang, J. Y. Wang, and M. H. Jiang, "Efficient diode-pumped

actively Q-switched Nd:YAG/$BaWO_4$ intracavity Raman laser," Opt. Lett. **30**(24), 3335–3337 (2005).

[19] G. M. Gad, H. J. Eichler, and A. A. Kaminskii, "Highly efficient 1.3-μm second-Stokes $PbWO_4$ Raman laser," Opt. Lett. **28**, 426-428 (2003).

[20] W. Chen, Y. Inagawa, T. Omatsu, M. Tateda, N. Takeuchi, Y. Usuki, "Diode-pumped, self-stimulating, passively Q-switched $Nd^{3+}$: $PbWO_4$ Raman laser," Opt. Commun. **194**, 401-407 (2001).

[21] A. Kaminskii, C. McCray, H. Lee, S. Lee, D. Temple, T. Chyba, W. Marsh, J. Barnes, A. Annanenkov, V. Legunet, H. Eichler, G. Gad, and K. Ueda, "High efficiency nanosecond Raman lasers based on tetragonal $PbWO_4$ crystals," Opt. Commun. **183**, 277-287 (2000).

[22] J.T., Murray, W.L., Austin, and Powell, R.C., "Intracavity Raman conversion and Raman beam cleanup," Opt. Mater. **11**(4), 353-371(1999).

[23] Y. Ma, A. Vallés, J.C. Tung, Y.F. Chen, K. Miyamoto, and T. Omatsu, "Direct generation of red and orange optical vortex beams from an off-axis diode-pumped $Pr^{3+}$: YLF laser," Opt. Express **27**, 18190-18200 (2019).

[24] D. J. Kim and J. W. Kim, "Direct generation of an optical vortex beam in a single-frequency Nd: $YVO_4$ laser," Opt. Lett. **40**, 399-402 (2015).

[25] Igor A. Litvin, Sandile Ngcobo, Darry Naidoo, Kamel Ait-Ameur, and Andrew Forbes, "Doughnut laser beam as an incoherent superposition of two petal beams," Opt. Lett. **39**, 704-707 (2014).

[26] T. Omatsu, K. Miyamoto, A. J. Lee, "Wavelength-versatile optical vortex lasers," J. Opt. **19**, 123002 (2017).

[27] J. W. Kim, J. I. Mackenzie, J. R. Hayes, and W. A. Clarkson, "High power Er:YAG laser with radially-polarized Laguerre-Gaussian ($LG_{01}$) mode output," Opt. Express **19**, 14526-14531 (2011).

[28] D. J. Kim, J. W. Kim, and W. A. Clarkson, "Q-switched Nd:YAG optical vortex lasers," Opt. Express **21**, 29449-29454 (2013).

[29] D. Lin, J. M. O. Daniel, and W. A. Clarkson, "Controlling the handedness of directly excited Laguerre–Gaussian modes in a solid-state laser," Opt. Lett. **39**, 3903-3906 (2014).

# 6. Visible vortex beams generation from a diode-pumped $Pr^{3+}$:YLF laser

In this chapter, the development of visible vortex laser sources, based on diode-pumped $Pr^{3+}$:YLF lasers with an off-axis pumping geometry, is presented. The systems enable the efficient generation and the handedness control of the optical vortex modes in the visible region (607 nm and 640 nm).

## 6.1 Introduction

Visible vortex sources potentially enable the development of laser micro-fabrication systems and super-resolution fluorescence microscopes, because many materials exhibit strong absorption bands in the visible region.

$Pr^{3+}$ doped solid-state laser crystals exhibit excellent emission transitions in the visible spectral region [1], including green (523 nm), orange (607 nm), red (640 nm), dark-red (720 nm). Also, they have strong absorption bands in the blue region (~ 442 nm), thereby allowing a blue indium gallium nitride (InGaN) laser diode pumping. In recent years, several research groups have successfully developed diode-pumped, continuous-wave [2], Q-switched [3], and mode-locked $Pr^{3+}$:YLF lasers [4]. Going beyond these previous $Pr^{3+}$:YLF laser works, the development of visible LG laser sources is still a challenge.

In this work, I propose a visible vortex laser source based on a diode-pumped $Pr^{3+}$:YLF laser with an off-axis pumping geometry. Maximum LG mode powers of 808 mW and 211 mW were achieved at the wavelengths of 640 nm and 607 nm. This system also allows the direct generation of versatile structured light beams given by the coherent superposition of the orthogonal HG modes.

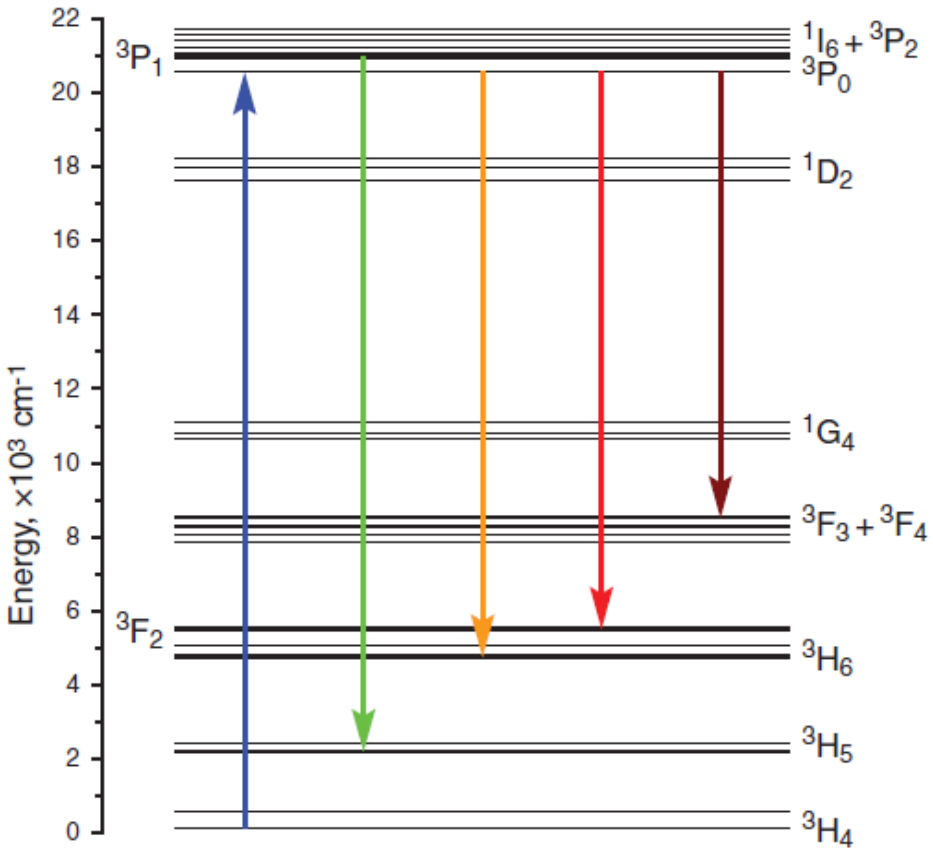


Fig. 6.1 Energy level diagram of the $Pr^{3+}$ ion in fluoride crystals [1].

## 6.2 Experiments

Experimental setup for the visible vortex laser is shown in Fig. 6.2(a). The gain medium used was a *a*-cut YLF crystal (dimensions of 3 × 3 × 5 $mm^3$) with 0.5 at.% $Pr^{3+}$-doping, and its temperature was maintained to be ~15 $^{o}$C by a circulating water-cooled chiller. It also exhibited the absorption peak for the σ-polarization at 442 nm. Thus, a 3.5 W InGaN laser diode (NDB7K75) with a wavelength of 440 ~ 455 nm was used as a pump source, thereby maximizing absorption of the crystal [1]. The pump diode beam was collimated by an aspheric lens ($f$ = 4.51 mm) and a cylindrical lens ($f$ = 250 mm), and it was then focused to be an elliptical beam spot with approximate dimensions of 100×40 $\mu m^2$ onto the input facet of the crystal by a plano-convex lens ($f$ = 35 mm).

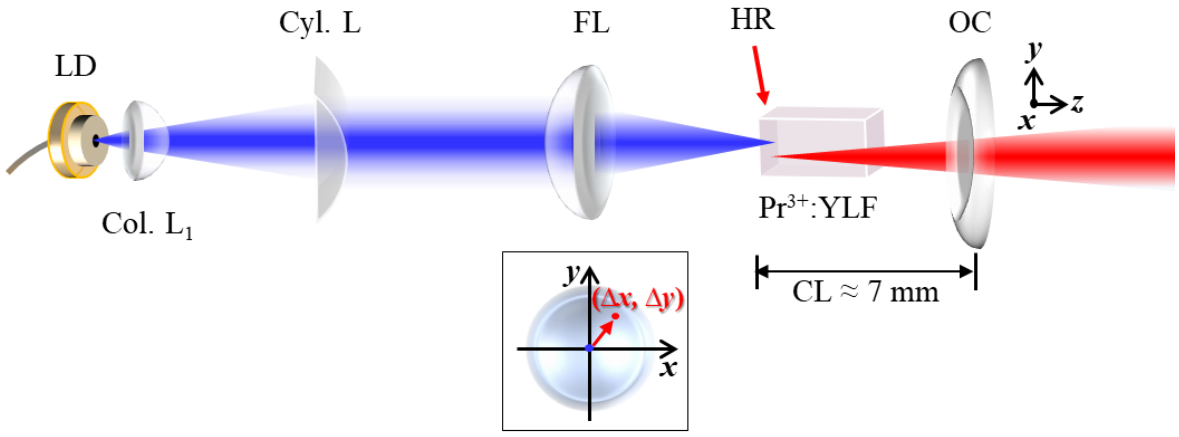


Fig. 6.2 Diode-pumped $Pr^{3+}$:YLF vortex laser source formed of an off-axis pumping configuration. LD: Blue InGaN laser diode; Col. $L_1$: collimated lens ($f$ = 4.51 mm); Cyl. L: cylindrical lens ($f$ = 250 mm); FL: focusing lens ($f$ = 35 mm); HR: high-reflection coating at the wavelengths of 640 nm or 607 nm; CL: cavity length; OC: output coupler. The inset represents the OC displacements along $x$ and $y$ axes for an off-axis pumping configuration.

It is worth noting that two crystals with different coatings were used, so that the system lases at a wavelength of 640 nm (red) or 607 nm (orange). The first crystal was used for 640 nm lasing, and its input facet had reflectivities of 99.8 % and 98.3 % at 640 nm and 607 nm. The second crystal was used for 607 nm lasing, and its input facet showed reflectivities of 92.6 % and 99.6 % at 640 nm and 607 nm. The output facets of both crystals were also anti-reflection coated for 640 nm, 607 nm, and 442 nm. The cavity consisted of the crystal input facet and a 150 mm concave output coupler (OC) with high reflections (R = 98.7%, 98.8%) for 640 nm and 607 nm, as shown in Fig. 6.2. The OC then was 2-dimensionally translated along the $x$ and $y$ axes with 0.5 μm steps, thereby allowing the optimization of the spatial mode overlap efficiency between the desired laser mode and pump beam in the off-axis pumping configuration (see the inset of Fig. 6.2). The handedness of the generated laser output was then assigned by the fork-shaped fringes, in which a pair of upward/downward (downward/upward) fringes is defined as $\ell = +1$ (right-handed) or $\ell = -1$ (left-handed).

Figure 6.3 indicates the experimental lasing spectrum of the generated red (640 nm) and orange (607 nm) vortex outputs. The vortex outputs typically showed a perfect annular

spatial form as shown in Fig. 6.4. The cavity length then was fixed to be approximately 7 mm. It is also worth mentioning that the vortex beams were produced even in further extended cavity configurations (~ 20 mm), but the system became slightly unstable.

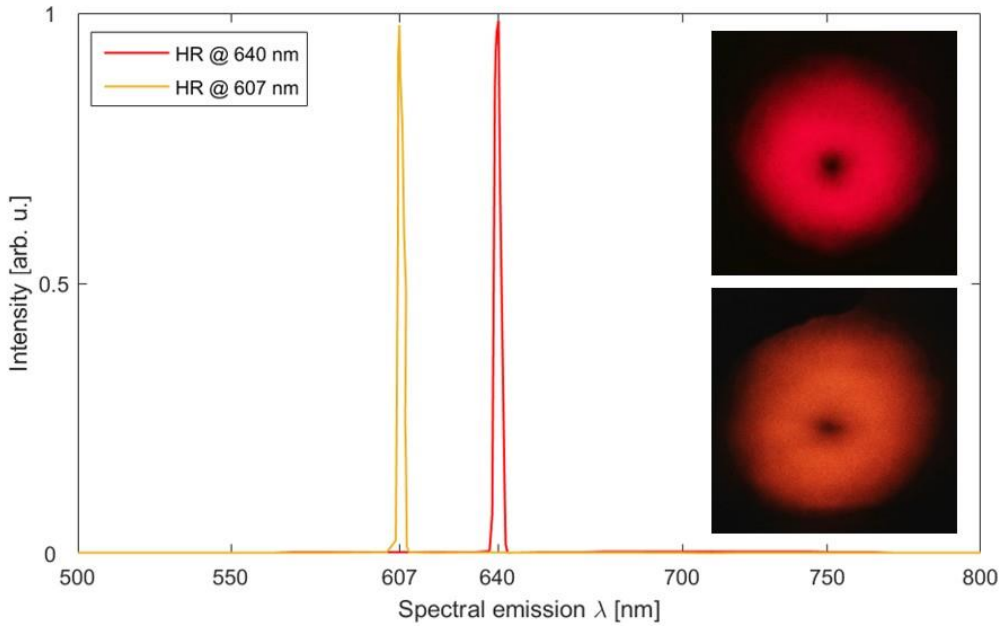


Fig. 6.3 Normalized lasing spectra of the optical vortex mode generated from the system with two different crystals. The insets represent real pictures of the red and orange vortex beams generated from the system.

## 6.3 Results and discussions

The laser operated at Gaussian mode under an on-axially pumping. This OC position was assumed to locate at the center of the coordinate system, ($x$, $y$) = (0,0) µm, and the spatial forms of the laser output were mapped as a function of OC position as shown in Fig. 6.4. This map allows us to identify the modes generated from the cavity under different off-axis pumping configurations. As shown in the inset of Fig. 6.2(a), the OC was then translated horizontally and vertically from the center of coordinates, with $\Delta x \approx \pm 12.5$ µm and $\Delta y \approx \pm 37.5$ µm steps, up to a maximum of ($x$, $y$) = (±25, ±75) µm. It is noteworthy that the spatial mode evolution obeys the principle of symmetry shown in Fig. 6.4.

As the increase of OC displacements from the center of coordinates, the laser output was

gradually transformed from a Gaussian mode to a doughnut-shaped LG mode via a mixed mode with two petals. When the off-axis displacements of the OC increased further, the laser output exhibited higher order Ince-Gaussian modes, as previously reported in [5].

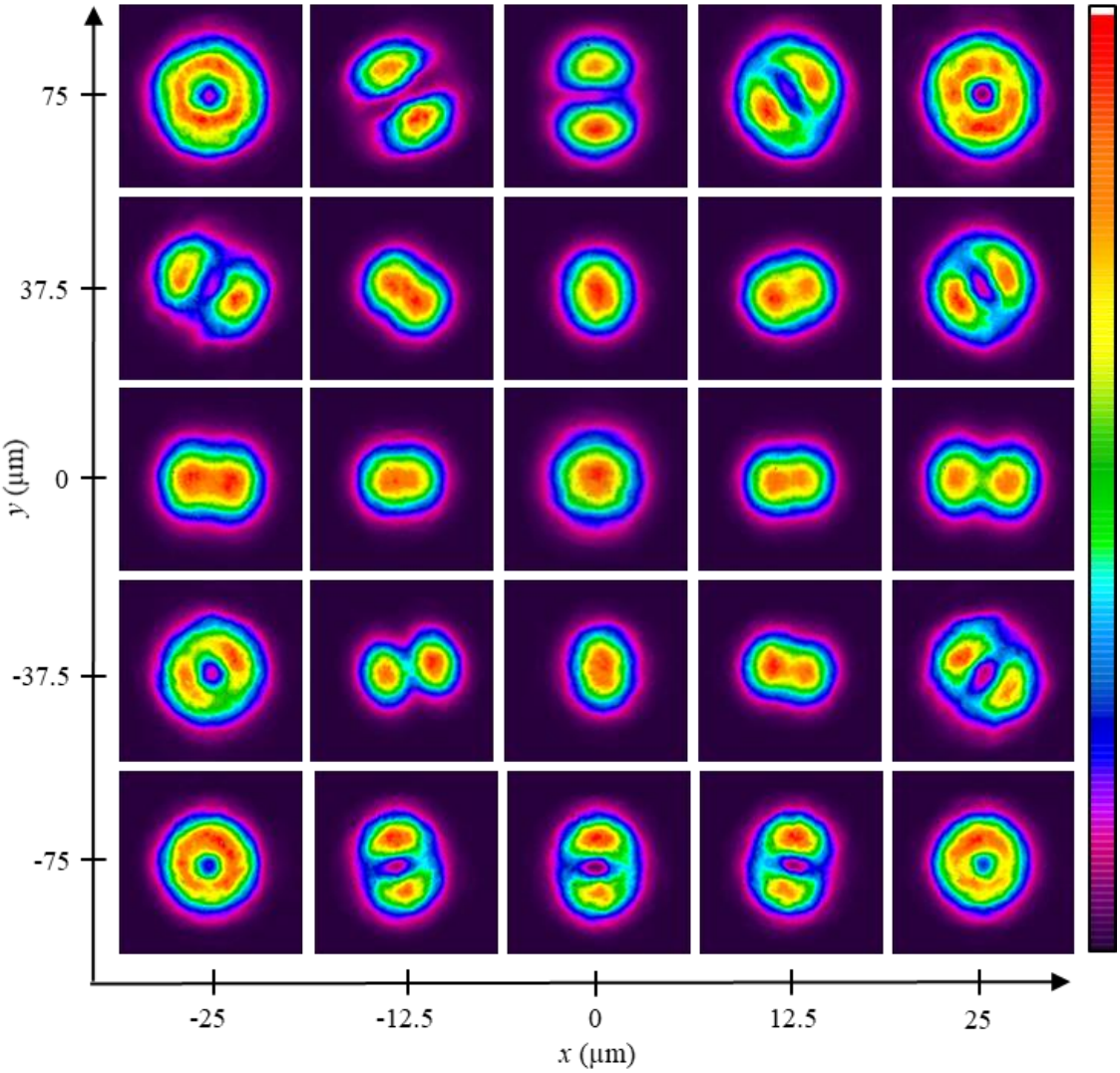


Fig. 6.4 Spatial mode mapping of the laser system with different OC displacements ($\Delta x \approx \pm 12.5$ μm and $\Delta y \approx \pm 37.5$ μm steps).

A pair of upward/downward (or downward/upward) Y-shaped fringes manifests the generation of the vortex beam with OAM mode $\ell = +1$ (or $\ell = -1$), as shown in Fig. 6.5. Such handedness control of the vortex beam can be realized simply by translating the OC from $(\pm 25, \pm 75)$ μm to $(\mp 25, \pm 75)$ μm and vice versa.

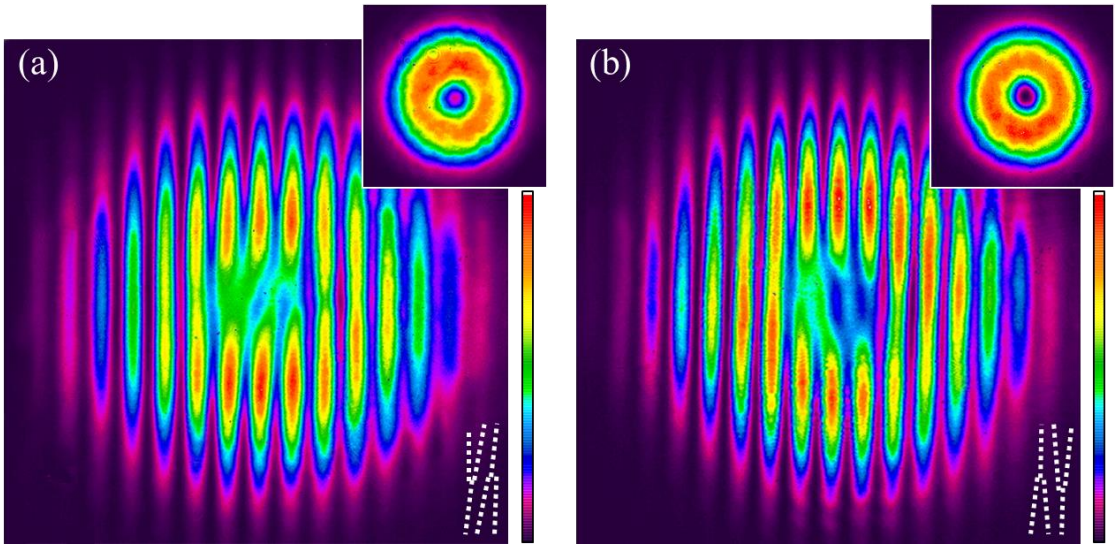


Fig. 6.5 Self referenced fringes of a (a) right-handed vortex beam (ℓ = +1), and (b) left-handed vortex beam (ℓ = -1). The OC positions were then (25, 75) and (-25, 75) μm. The insets represent the spatial forms for the generated vortex beams.

In fact, such generated mixed modes, $M_{out}(\theta, \varphi)$, should be decomposed of orthogonal HG modes ($HG_{m,n}$) with inter-modal relative phase [6], and thus, they can be expressed as follows:

$$M_{out}(\theta, \varphi) = \cos\theta \, HG_{0,1} + \exp(i\varphi) \sin\theta \, HG_{1,0} \tag{6.3.1}$$

, where $\varphi$ is the inter-modal phase, and $\theta$ represents the weighting factor for $HG_{0,1}$ and $HG_{1,0}$ modes, determined by the off-axis pumping geometry. Figure 6.6 shows versatile spatial modes experimentally generated at off-axis positions of the OC (upper rows), and the corresponding spatial forms (lower rows) simulated by employing Eq. (6.3.1) with the appropriate $\varphi$ and θ.

For instance, a generated mixed mode with two petals, as shown in Fig. 6.6(d), can be perfectly retrieved by using $\varphi = 0.37\pi$ and $\theta = \pi$ ($M_{out}(0.37\pi, \pi) = 0.40\, HG_{01} - 0.92\, HG_{10}$).

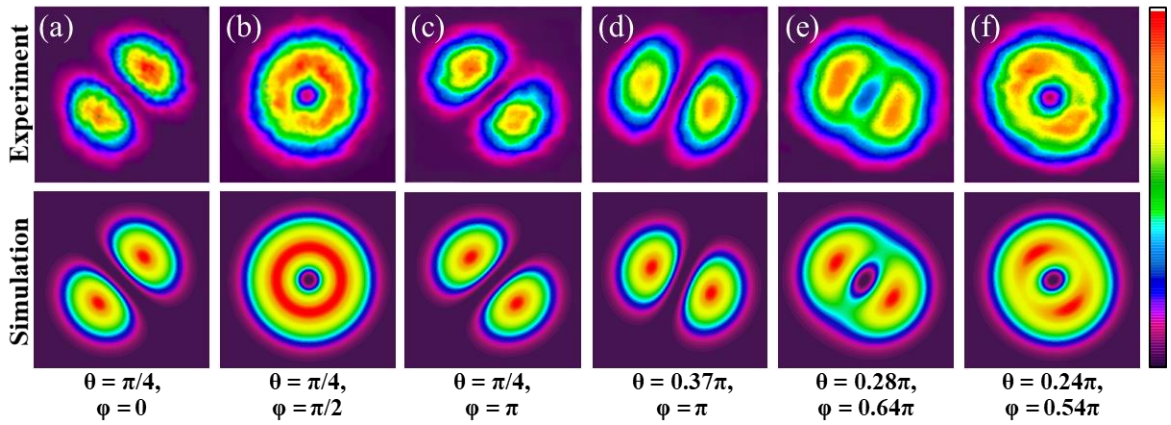


Fig. 6.6 Experimental (upper rows) and theoretical (lower rows) spatial modes obtained at different OC positions.

Also, a coherent superposition of orthogonal HG modes with same weighting factor and zero relative phase ($\theta = \pi/4$, $\varphi=0$) results in a 45° inclined twin mode (see Fig. 6.6(a)). Further, annular LG modes with OAM $\ell = \pm 1$ can be produced when $\theta = \pi/4$ and $\varphi=\pm\pi/2$ (see Fig. 6.6(b)) as follows:

$$\mathrm{LG}_{0,\pm1} = 1/\sqrt{2}\left(HG_{0,1} \pm i\, HG_{1,0}\right) \tag{6.3.2}$$

These manifest that the generated spatial modes in this system can be numerically retrieved by employing a coherent superposition as mentioned in eq. (6.3.1).

The maximum red and orange Gaussian output powers were measured to be 965 mW and 337 mW at a pump power of 3.16 W, corresponding to slope efficiencies of 33.7 % and 15.7 %, respectively. The red and orange vortex output powers ($\ell = \pm 1$) then reached up to 808 mW and 211 mW with slope efficiencies of 37.3 % and 16.7 % at the maximum pump level. The $Pr^{3+}$:YLF crystal exhibits the relatively weak emission ($13.6 \times 10^{-20}$ $cm^2$) for orange transition compared with that ($21.8 \times 10^{-20}$ $cm^2$) of the red transition, thus, the laser exhibited less slope efficiency and higher lasing threshold for 607 nm [8]. Figure 6.7 summarizes the power scaling of the $Pr^{3+}$:YLF laser system.

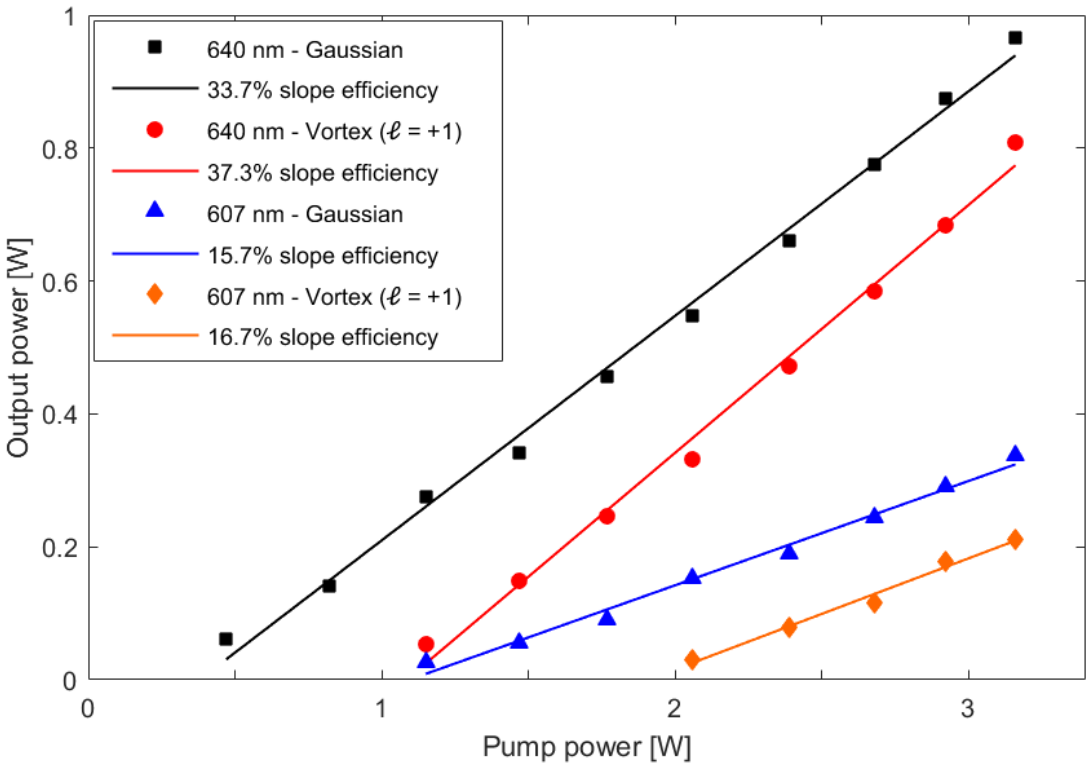


Fig. 6.7 Power scaling of the laser system.

## 6.4 Conclusion

Red (640 nm) and orange (607 nm) vortex modes have been directly generated from a diode-pumped $Pr^{3+}$:YLF laser with an off-axis pumping configuration. The generated vortex modes can be fully characterized by a coherent superposition of orthogonal HG modes with different amplitudes and relative phases. Also, the selective handedness control of the vortex beam is achieved only by laterally displacing the OC. Red (640 nm) and orange (607 nm) vortex output powers of 808 mW and 211 mW were observed at a pumping power of 3.16 W. Such compact visible vortex laser sources can potentially explore advanced technologies, such as fluorescence microscopes and micro-fabrications with high spatial resolution beyond the diffraction limit.

## 6.5 References

[1] X. Li, X. Yu, R. Yan, R. Fan, and D. Chen, "Optical and laser properties of $Pr^{3+}$:YLF crystal," Laser Phys. Lett. **8**, 791 (2011).

[2] T. Gün, P. Metz, and G. Huber, "Power scaling of laser diode pumped $Pr^{3+}$: $LiYF_4$ CW lasers: efficient laser operation at 522.6 nm, 545.9 nm, 607.2 nm, and 639.5 nm," Opt. Letters **36**, 1002–1004 (2011).

[3] H. Tanaka, R. Kariyama, K. Iijima, K. Hirosawa, and F. Kannari, "Saturation of 640-nm absorption in $Cr^{4+}$: YAG for an InGaN laser diode pumped passively Q-switched $Pr^{3+}$: YLF laser," Opt. Express **23**, 19382–19395 (2015).

[4] K. Iijima, R. Kariyama, H. Tanaka, and F. Kannari, "$Pr^{3+}$:YLF mode-locked laser at 640 nm directly pumped by InGaN-diode lasers," Appl. Opt. **55**, 7782–7787 (2016).

[5] T. Ohtomo, K. Kamikariya, K. Otsuka, and S.-C. Chu, "Single-frequency Ince-Gaussian mode operations of laser-diode-pumped microchip solid-state lasers," Opt. Express **15**, 10705–10717 (2007).

[6] M. A. Bandres and J. C. Gutiérrez-Vega, "Ince–gaussian modes of the paraxial wave equation and stable resonators," JOSA A **21**, 873–880 (2004).

[7] A. Forbes, A. Dudley, and M. McLaren, "Creation and detection of optical modes with spatial light modulators," Adv. Opt. Photonics **8**, 200–227 (2016).

[8] S. Luo, X. Yan, Q. Cui, B. Xu, H. Xu, and Z. Cai, "Power scaling of blue-diode-pumped Pr: YLF lasers at 523.0, 604.1, 606.9, 639.4, 697.8 and 720.9 nm," Opt. Commun. **380**, 357–360 (2016).

[9] M. Okida, T. Omatsu, M. Itoh, and T. Yatagai, "Direct generation of high power Laguerre-gaussian output from a diode-pumped Nd: $YVO_4$ 1.3-μm bounce laser," Opt. Express **15**, 7616–7622 (2007).

# 7. Bottle beams generated from a frequency-doubled Nd:$YVO_4$ laser

In this chapter, the direct generation of bottle beams with high optical potential barriers from a compact frequency-doubled Nd:$YVO_4$ laser with a nearly hemispherical configuration is presented. Also, the theoretical analysis, based on the frequency-doubling of radial-order LG modes, is addressed. Such bottle beams will be potentially utilized in 3D optical trapping for light-absorption particles and fluorescence microscopes with high 3D spatial resolution.

## 7.1 Introduction

Freegarde et.al proposed theoretically that the superposition of higher order radial LG beams enable the generation of bottle beams with high optical potential barrier [1]. Intriguingly, the direct generation of higher order radial LG modes from an end-pumped solid-state laser with a nearly hemispherical cavity and a tightly focused pumping configurations [2] has also been reported. Also, it has been theoretically and experimentally reported that the frequency-doubled radial-order LG mode with radial index $p$ exhibits a coherent superposition of radial-order LG modes with radial indies $2p'$ for $p' = 0,1, \dots, p$ [3].

In this chapter, I present the direct generation of bottle beams with high optical potential barrier from a frequency-doubled Nd:$YVO_4$ laser with a hemispherical cavity and a tightly focused pumping configurations. The generated bottle beam, formed of the coherent superposition of frequency-locked radial LG modes, exhibits a 3D dark core in the intermediate region between the near and far fields, and it also has several times higher optical potential barrier than that mentioned previously [3,4].

## 7.2 Experiments

The laser cavity consisted of a 30-mm concave mirror with high reflection for 1064 nm (R > 99.8%) and high transmission (T > 95%) for 808 nm, and a 98% reflective flat OC

for 1064 nm. The cavity length was then designed to be ~29.2 mm for a hemispherical cavity configuration. An *a*-cut 2.0 at.% Nd:$YVO_4$ crystal with a length of 2 mm and an aperture of 10×10 $mm^2$ was used for a laser gain medium, and its apertures were anti-reflection coated for 1064 nm (R < 0.2%). The crystal was mounted on a water-cooled copper block to ensure stable laser operation. Tightly focused pumping configuration requires that the pump spot radius should be considerably smaller than that of the cavity mode in the gain medium. To satisfy this condition, the crystal was placed within a distance of 1 mm from the concave mirror. The cavity mode radius was then estimated to be ~240 μm. A 3.0 W 808 nm fiber-coupled laser diode (a core diameter: 100 μm, NA: 0.16) was used for a pump source, and its output was tightly focused to be a spot with a radius of 25 μm on the crystal.

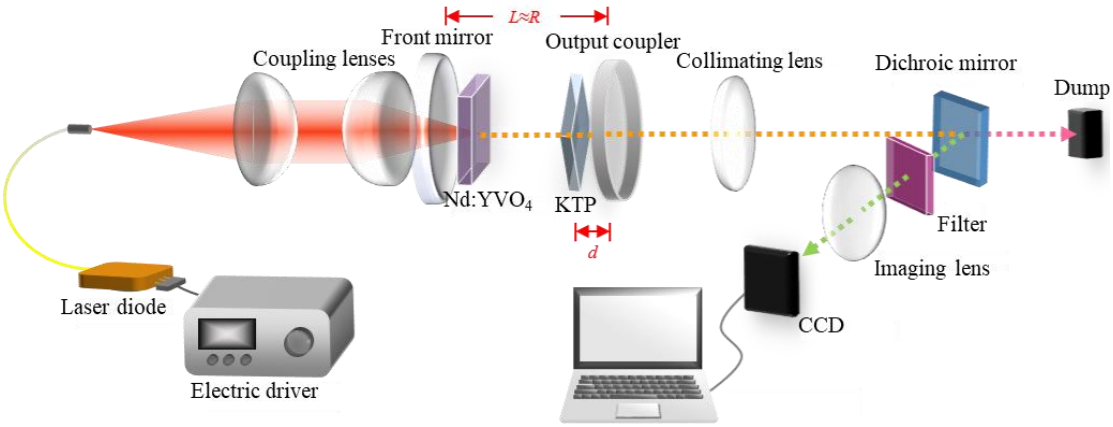


Fig. 7.1 Bottle beam generation from a diode-pumped, frequency-doubled Nd:$YVO_4$ laser with a nearly hemispherical cavity configuration.

This system allows us to generate the radial LG mode with $p = 1$ within the pump power region of 1.75–2.40 W (yellow zone), as shown in Fig. 7.2. It is worth mentioning that this radial LG mode should include undesired Gaussian mode as an impurity owing to the frequency-locking effects between the transverse and longitudinal modes of the hemispherical cavity [2]. Such mixed mode operation of the system acts as an important role to generate a bottle beam with a high optical potential

barrier. The output power of 130–150 mW was then obtained within a pump power region of 1.75–2.40 W.

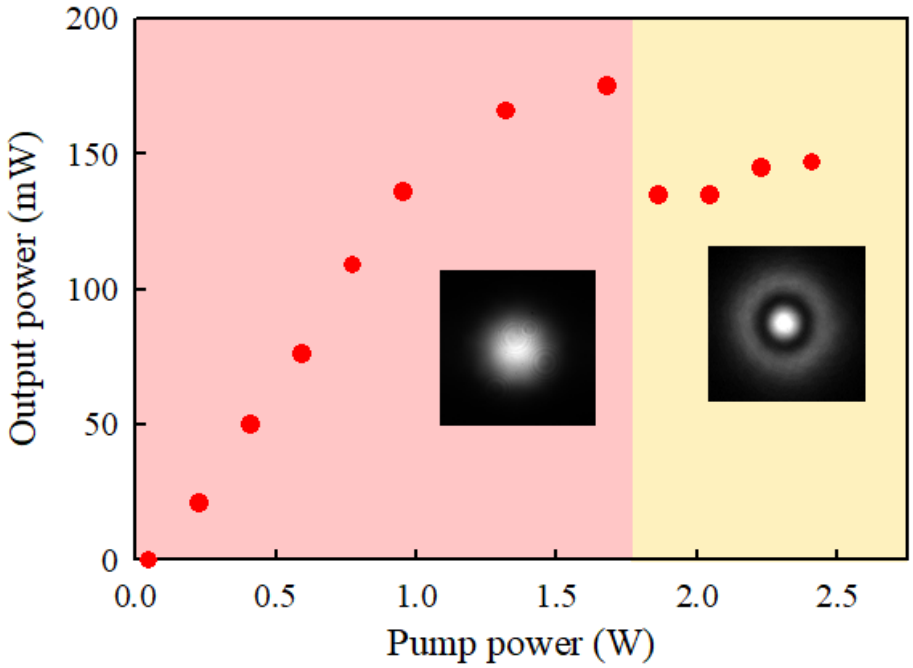


Fig. 7.2 Output powers versus pump powers. The insets represent the spatial forms of fundamental outputs.

To perform efficient intracavity SHG, the OC was replaced by an OC with high reflection for 1064 nm (R>99.8%). Also, a type-II phase matching $KTiPO_4$ (KTP) crystal (thickness: 1 mm, aperture: 10×10 $mm^2$) was placed near the OC with the distance of $d$ shown in Fig. 7.1. Both faces of the KTP were anti-reflection coated for both the fundamental (R<0.2%@1064 nm) and the second-harmonic wavelengths (R<0.2%@532 nm). The generated second harmonics was delivered by a relay optics towards a CCD camera mounted onto a translation stage.

When $d \approx 1.0$ mm, that is the KTP was placed near the OC, the generated second harmonics showed typically the beam propagation of a bottle beam, namely central bright spots appeared in the near and far fields, and a well-isolated dark core surrounded by a bright ring-shaped optical field was seen in the intermediate between the near and far fields, as shown in the upper row of Fig. 7.3(a) (Rayleigh length $z_R \approx 4.8$ mm).

The bottle beam was produced within the pump power region of 2.0–2.4 W (yellow

zone) in Fig. 7.3 (d), and its maximum output power of 13.2 mW was then measured at a pump power of 2.0 W. It will be possible to further scale the output power by refinements of the cavity design and optimization of the thickness of KTP crystal.

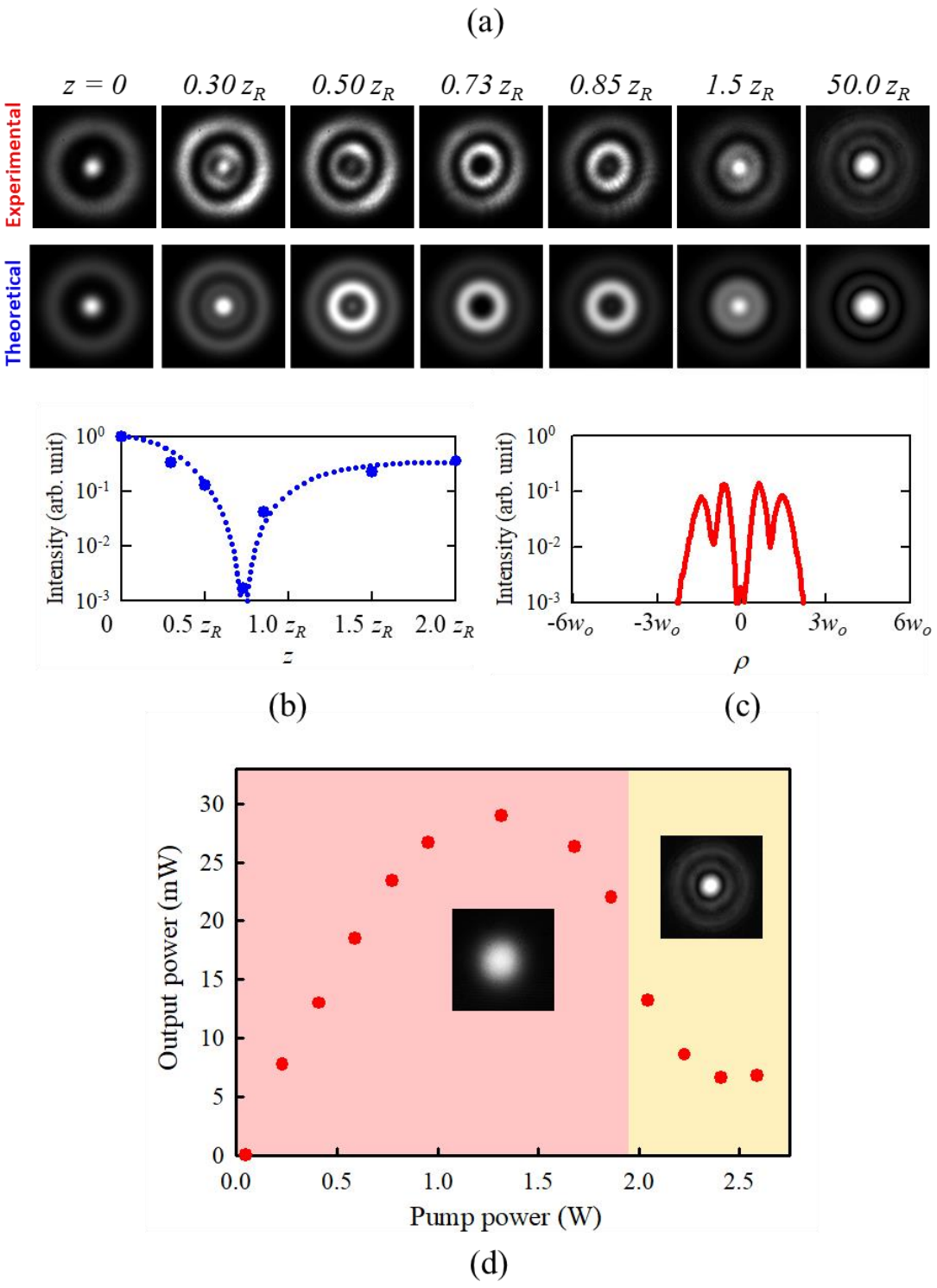


Fig. 7.3 (a) Upper row: experimental beam propagation of the generated bottle beam at different longitudinal positions. Lower row: theoretical beam propagation for

comparison. (b,c) Experimental intensity profiles of the generated bottle beam along with the propagation and radial directions. (d) Experimental output powers and spatial forms versus pump powers.

## 7.3 Discussion

The wave function of radial-order LG modes $\Phi_{p,s}(\rho,\phi,z,\varphi)$ with radial mode index $p$ and longitudinal mode index $s$ in cylindrical coordinates $(\rho,\phi,\mathrm{z})$ is given by [5]

$$\Phi_{p,s}(\rho,\phi,z,\varphi)=\sqrt{\frac{1}{\pi}}\frac{1}{w(z)}L_p\left(\frac{2\rho^2}{w^2(z)}\right)e^{-\rho^2/w^2(z)}e^{-ik_{p,s}\tilde{z}}e^{i(2p+1)\,[\theta_G(z)+\,\varphi]}\ , \quad (7.3.1)$$

where

$$\tilde{z}=z+[\frac{z\rho^2}{2\,(z^2+z_R^2)}], \quad (7.3.2)$$

$$w(z)=w_o\sqrt{1+(\frac{z}{z_R})^2}, \quad (7.3.3)$$

$$\theta_G(z)=tan^{-1}\left(\frac{z}{z_R}\right), \quad (7.3.4)$$

and

$$z_R=\pi {w_o}^2/\lambda. \quad (7.3.5)$$

where $L_p(\cdot)$is the $p^{\text{th}}$-order Laguerre polynomials, $w_o$ is the beam waist radius, λ is the wavelength, φ is the relative phase among transverse and longitudinal modes at $z$ = 0, and $k_{p,s}$ is the wavenumber. In terms of the effective cavity length $L$, the wave number $k_{p,s}$ is given by $k_{p,s}L=\pi[s+2p(\Delta f_T/\Delta f_L)]$ , where $\Delta f_L=c/2L$ is the longitudinal mode spacing and $\Delta f_T$ is the transverse mode spacing. It is found [6] that when the ratio $\Delta f_T/\Delta f_L$ is close to a simple fraction, the longitudinal transverse mode coupling effects should bring about the frequency locking phenomenon among different order transverse modes with the aid of different order longitudinal modes. For the present cavity configuration, $\Delta f_T/\Delta f_L\approx 1/2$, the fundamental lasing mode is formed by a family of frequency-degenerate LG modes $\Phi_{q,N-q}(\rho,\phi,z)$ with $q=$

$0,\ 1,\ 2,\ \ldots,\ p$ as follows:

$$u_p(\rho,\phi,z,\varphi) = \sum_{q=0}^{p} a_q\ \Phi_{q,N-q}(\rho,\phi,z,\varphi) \tag{7.3.6}$$

where $a_q$ is the amplitude of the radial LG mode with $q$. The summation $\sum_q a_q = 1$is then satisfied. Considering SHG, the frequency-doubled optical field is proportional to the square of the incident optical field [7]. Thus, the second-harmonic mode $\Psi_p(\rho,\phi,z)$ can be written by the square of the fundamental lasing mode:

$$\Psi_p(\rho,\phi,z) = \eta\left[\sum_{q=0}^{p} a_q\ \Phi_{q,N-q}(\rho,\phi,z)\right]^2. \tag{7.3.7}$$

where $\eta$ is the constant related to the effective second harmonic generation efficiency. The second-harmonic optical field of LG mode with $p$ =1 is given by

$$\Psi_1(\rho,\phi,z,\varphi) = \eta\left[a_0\ \Phi_{0,N}(\rho,\phi,z,\varphi) + a_1\ \Phi_{1,N-1}(\rho,\phi,z,\varphi)\right]^2. \tag{7.3.8}$$

Here,

$$\left[\Phi_{0,N}(\rho,\phi,z,\varphi)\right]^2 = \xi\Phi'_{0,N}(\rho,\phi,z,\varphi), \tag{7.3.9}$$

$$\Phi_{0,N}(\rho,\phi,z,\varphi)\Phi_{1,N-1}(\rho,\phi,z,\varphi) = (\xi/2)\left[\Phi'_{1,N-1}(\rho,\phi,z,\varphi) + \Phi'_{0,N}(\rho,\phi,z,\varphi)\right.$$

$$\left.e^{2\,i\,[\theta_G(z)+\,\varphi]}\right], \tag{7.3.10}$$

$$\left[\Phi_{1,N-1}(\rho,\phi,z,\varphi)\right]^2 = (\xi/2)\left[\Phi'_{2,N-2}(\rho,\phi,z,\varphi) + \Phi'_{0,N}(\rho,\phi,z,\varphi)e^{4\,i\,[\theta_G(z)+\,\varphi]}\right], \tag{7.3.11}$$

and

$$\xi = \frac{e^{i\,[\theta_G(z)+\,\varphi]}}{[2\sqrt{\pi}w'(z)]}. \tag{7.3.12}$$

where $w'_o = w_o/\sqrt{2}$ and $k' = 2k$.

The relationships

$$L_0(x)^2 = L_0(x), \tag{7.3.13}$$

$$L_0(x)L_1(x) = L_1(x), \tag{7.3.14}$$

$$L_1(x)^2 = 2L_2(x) - 2L_1(x) + L_0(x), \tag{7.3.15}$$

And from the formulas [8,9]

$$L_u(x) = \frac{1}{2^u}\sum_{m=0}^{u} \frac{u!}{(u-m)!m!} L_{u-m}\,(2x), \tag{7.3.16}$$

are then used.

The second-harmonic optical field can, thus, be expressed by

$$\Psi_1(\rho,\phi,z,\varphi) = \eta'\big[b_0\ \Phi'_{0,N}(\rho,\phi,z,\varphi) + b_1\ \Phi'_{1,N-1}(\rho,\phi,z,\varphi) + b_2\ \Phi'_{2,N-2}(\rho,\phi,z,\varphi)\big], \tag{7.3.17}$$

where $b_0 = {a_0}^2 + a_0a_1e^{2\,i\,[\theta_G(z)+\,\varphi]} + ({a_1}^2/2)e^{4\,i\,[\theta_G(z)+\,\varphi]}$, $b_1 = a_0a_1$, and $b_2 = {a_1}^2/2$.

The relative phase $\varphi$ between the transverse and longitudinal modes was determined to be 0, arising from the large acceptance bandwidth (~220 nm) of the KTP crystal [10]. Thus, the mode components $a_0$ and $a_1$ were then assigned to be 0.29 and 0.71, respectively, to retrieve the experimental beam propagation of the generated bottle beam, as shown in the lower row of Fig. 7.3(a). Also, note that the non-zero relative phase $\varphi$ should be considered with the increase of *d*, that is as the KTP is moved away from the OC.

There is a good agreement between theoretical analysis and experiments, in which the generated second harmonics exhibits a well-isolated and narrow 3D dark spot surrounded by a bright optical field in the intermediate region between the near and far fields (Fig. 7.3(a)). Such a bottle beam is generated by constructive or deconstructive interference of three radial LG modes with *p* of 0–2 owing to Gouy-phase shift effects. Its potential hill slope along the propagation direction was defined as the intensity difference of two maximal points divided by the distance between two maximal points, and it was estimated to be 0.071 $z_R^{-1}$. These suggest that this bottle beam with a high optical potential barrier will enable the 3D trapping of light-absorptive particles [11,12].

The experimental second harmonics at $d$ =1.8 mm showed a far-field with a dark core and a near-field with a bright spot, owing to ~π/4 dephasing between $\Phi_{0,N}$ and $\Phi_{1,N-1}$, thereby losing the properties of a bottle beam. The second harmonics also exhibited a near-field with a central bright spot and a far-field with a dark core. These experiments are well supported by theoretical analysis.

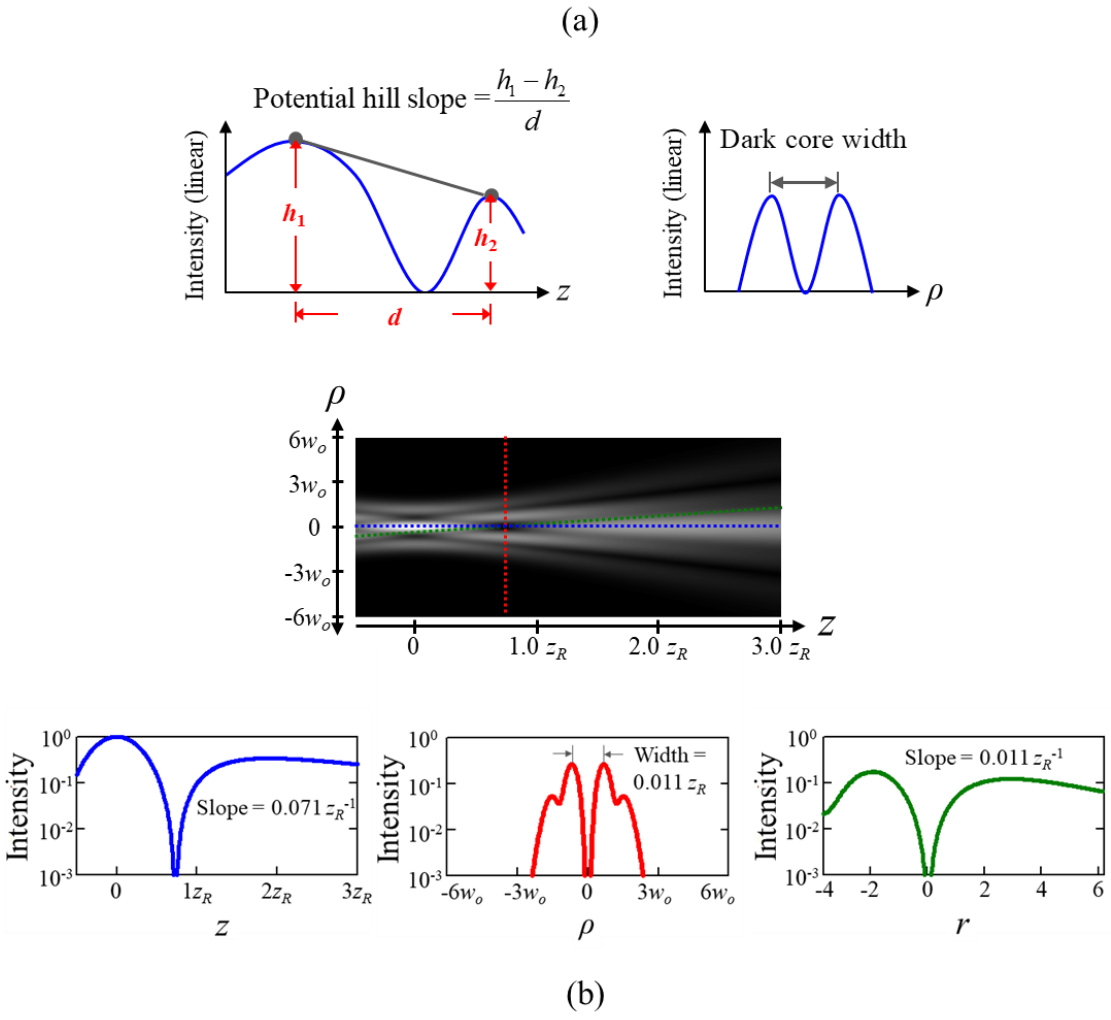


Fig. 7.4 (a) Definitions of potential hill slope and dark core width of the generated bottle beam. Simulated 2D spatial evolution and corresponding spatial forms along propagation, radial, and minimum intensity directions. (b) Lower row of the generated bottle beam in the present system.

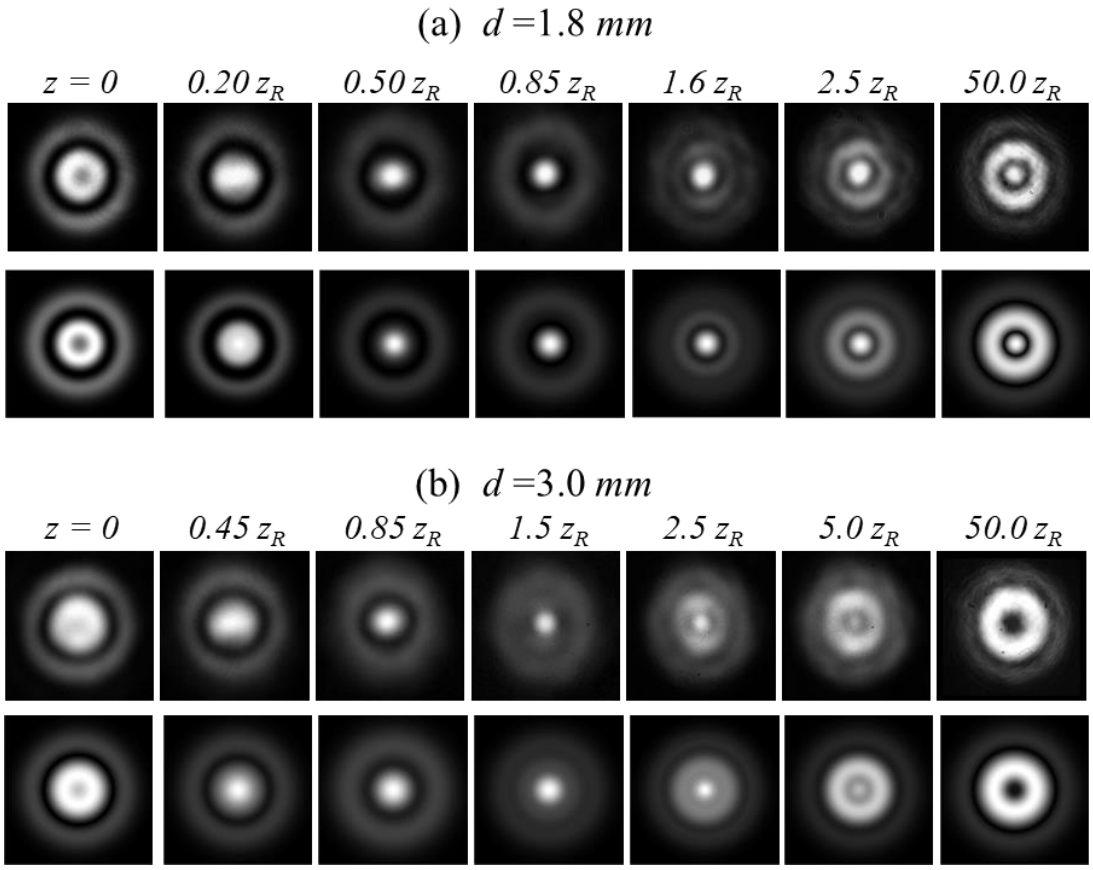


Fig. 7.5 Experimental (upper row) and simulated (lower row) beam propagtions of the bottle beam for (a) $d$ = 1.8 mm and (b) $d$ = 3.0 mm.

## 7.4 Conclusion

A bottle beam has been successfully produced from an intracavity frequency-doubled Nd:$YVO_4$ laser possessing a nearly hemispherical cavity configuration. The generated bottle beam showed a well-isolated and narrower 3D dark core with high optical potential barrier [3,4]. Furthermore, the beam propagation of the generated bottle beam can be theoretically addressed by the coherent superposition of frequency-locked radial LG modes.

## 7.5 References

[1] T. Freegarde and K. Dholakia, “Cavity-enhanced optical bottle beam as a mechanical amplifier,” Phys. Rev. A **66**, 013413 (2002).

[2] J. C. Tung, Y. H. Hsieh, T. Omatsu, K. F. Huang, and Y. F. Chen, “Generating laser transverse modes analogous to quantum Green’s functions of two-dimensional harmonic oscillators,” Photonics Res. **5**, 733-739 (2017).

[3] J. Courtial, K. Dholakia, L. Allen, and M. J. Padgett, “Second-harmonic generation and the conservation of orbital angular momentum with high-order Laguerre-Gaussian modes,” Phys. Rev. A **56**, 4193-4196 (1997).

[4] P. T. Tai, W. F. Hsieh, and C. H. Chen, “Direct generation of optical bottle beams from a tightly focused end-pumped solid-state laser,” Opt. Express **18**, 5827-5833 (2004).

[5] A. E. Siegman, Lasers (Mill Valley, CA: University Science Books, 1986)

[6] Y. F. Chen, T. H. Lu, K. W. Su, and K. F. Huang, “Devil’s staircase in three-dimensional coherent waves localized on Lissajous parametric surfaces,” Phys. Rev. Lett. **96**(21), 213902 (2006).

[7] A. Yariv, P. Yeh, Photonics: Optical Electronics in Modern Communications, 6th ed. (Oxford Univ. Press, New York, 2007) Chap. 8.

[8] H. Kleindienst and A. Lüchow, “Multiplication theorems for orthogonal polynomials,” Int. J. Quantum Chem. **48**, 239-247 (1993).

[9] M. Abramowitz, and I. A. Stegun, Handbook of Mathematical Functions (Dover, New York, 1970).

[10] T. Y. Fan, C. E. Huang, B. Q. Hu, R. C. Eckardt, Y. X. Fan, R. L. Byer, and R. S. Feigelson, “Second harmonic generation and accurate index of refraction measurements in flux-grown $KTiOPO_4$,” Appl. Opt. **26,** 2390-2394 (1987).

[11]T. A. Nieminen, V. L. Y. Loke, A. B. Stilgoe, G. Knöner, A. M. Brańczyk, N. R. Heckenberg, and H. Rubinsztein-Dunlop, “Optical tweezers computational toolbox,” J. Opt. A **9**, S196–S203 (2007).

[12]J. S. T. Gongora, and A. Fratalocchi, “Optical force on diseased blood cells: towards the optical sorting of biological matter”, Opt. Laser Eng. **76**, 40-44 (2016).

# 8. Conclusion

## 8.1 Thesis summary

I have successfully demonstrated the direct generation of infrared/visible LG beams and visible bottle beam from the solid-state laser source.

Firstly, a continuous-wave self-Raman Nd:$GdVO_4$ LG mode laser source has been demonstrated by employing a shaped pumping geometry formed of an axicon lens and a focusing lens. The LG mode operation of 1108 nm or 1173 nm, or both 1108 nm and 1173 nm was selectively achieved simply by adjusting the OC.

Secondly, the red (640 nm) and orange (607 nm) vortex beams have been directly generated from a diode end-pumped $Pr^{3+}$:YLF laser possessing an off-axis pumping scheme. This system also enables us to generate versatile structured light fields representing a coherent superposition of HG modes with different amplitudes and phases.

Thirdly, the bottle beams, consisting of the superposition of different radial LG modes, has been produced from a frequency-doubled Nd:$YVO_4$ laser with a tightly focused pumping and a nearly hemispherical cavity configurations.

## 8.2 Future work_ frequency extension of ultraviolet vortex laser sources

The aforementioned structured light laser sources can be extended to develop UV structured light sources via nonlinear frequency conversion.

For instance, the UV (261 nm, 304nm, 320 nm, and 360nm) vortex sources based on an intracavity frequency-doubled $Pr^{3+}$:YLF vortex laser with a β–$BaB_2O_4$ (BBO) crystal will be developed, as described in Fig. 8.1. These UV vortex laser sources will explore advanced technologies, such as micro-fabrication and scanning microscopes with high spatial resolution far beyond the diffraction limit.

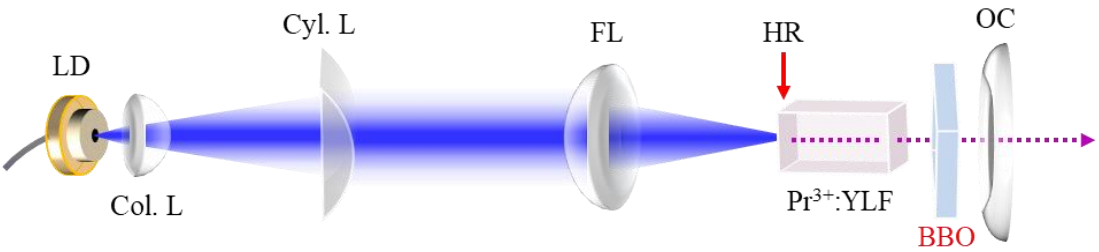


Fig. 8.1 UV $Pr^{3+}$:YLF vortex laser.

## 8.3 References

[1] A. Richter, N. Pavel, E. Heumann, G. Huber, D. Parisi, A. Toncelli, M. Tonelli, A. Diening, and W. Seelert, "Continuous-wave ultraviolet generation at 320 nm by intracavity frequency doubling of red-emitting Praseodymium lasers," Opt. Express **14**, 3282-3287 (2006).

[2] J. Kojou, Y. Watanabe, Y. Kojima, H. Nemoto, and F. Kannari, "Intracavity second-harmonic generation at 320 nm of an actively Q-switched Pr:$LiYF_4$ laser," Appl. Opt. **51**, 1382-1386 (2012).

[3] N. Niu, S. Pu, Q. Chen, Y. Wang, Y. Zhao, W. Wu, and Q. Zheng, "302 nm continuous wave generation by intracavity frequency doubling of a diode-pumped Pr: YLF laser," Appl. Opt. **57**(33), 9798-9802 (2018).